










Determinants of epigenetic resistance to HDAC inhibitors in dystrophic fibro-adipogenic progenitors

Silvia Consalvi^{1,2,*†} , Luca Tucciarone^{1,†}, Elisa Macri¹ , Marco De Bardi¹ , Mario Picozza¹ , Illari Salvatori^{1,3}, Alessandra Renzini⁴ , Sergio Valente⁵ , Antonello Mai⁵ , Viviana Moresi^{4,6}  & Pier Lorenzo Puri^{7,**} 

Abstract

Pharmacological treatment of Duchenne muscular dystrophy (DMD) with histone deacetylase inhibitors (HDACi) is currently being tested in clinical trials; however, pre-clinical studies indicated that the beneficial effects of HDACi are restricted to early stages of disease. We show that FAPs from late-stage mdx mice exhibit aberrant HDAC activity and genome-wide alterations of histone acetylation that are not fully reversed by HDACi. In particular, combinatorial H3K27 and/or H3K9/14 hypo-acetylation at promoters of genes required for cell cycle activation and progression, as well as glycolysis, are associated with their downregulation in late-stage mdx FAPs. These alterations could not be reversed by HDACi, due to a general resistance to HDACi-induced H3K9/14 hyperacetylation. Conversely, H3K9/14 hyper-acetylation at promoters of Senescence Associated Secretory Phenotype (SASP) genes is associated with their upregulation in late-stage mdx FAPs; however, HDACi could reduce promoter acetylation and blunt SASP gene activation. These data reveal that during DMD progression FAPs develop disease-associated features reminiscent of cellular senescence, through epigenetically distinct and pharmacologically dissociable events. They also indicate that HDACi might retain anti-fibrotic effects at late stages of DMD.

Keywords duchenne muscular dystrophy; FAPs; fibrosis; HDAC; regeneration
Subject Categories Chromatin, Transcription & Genomics; Molecular Biology of Disease; Stem Cells & Regenerative Medicine

DOI 10.15252/embr.202254721 | Received 24 January 2022 | Revised 24 February 2022 | Accepted 23 March 2022 | Published online 4 April 2022

EMBO Reports (2022) 23: e54721

Introduction

Duchenne muscular dystrophy (DMD) is a fatal genetic disease caused by lack of dystrophin (dys) expression (Hoffman *et al*, 1987; Muntoni *et al*, 2003). Genetic correction by restoration of dys expression with gene therapy approaches (Chamberlain & Chamberlain, 2017; Min *et al*, 2019; Verhaart & Aartsma-Rus, 2019) is predicted to recover the biochemical and functional integrity of the dystrophin-associated protein complex (DAPC) (Ervasti, 2006) and thereby protect myofiber sarcolemma stability post-contraction (Lapidos *et al*, 2004). However, a variety of “secondary” pathogenic events caused by dys deficiency can contribute to DMD progression (Constantin, 2014; Garbincius & Michele, 2015; Bhat *et al*, 2017; Morikawa *et al*, 2017; Hardee *et al*, 2021; Rugowska *et al*, 2021) and might persist even after gene therapy. Targeting these DMD-associated “secondary” events might therefore be necessary to achieve complete and long-lasting therapeutic recovery in DMD patients.

Among the “secondary” events caused by dys deficiency, pathogenic activation of specific sub-populations of muscle resident cells is emerging as key event in DMD progression (Serrano & Muñoz-Cánoves, 2017; Cappellari *et al*, 2020). Recent works have lent further support to the activation of “secondary” pathogenic responses in cell types that do not express dys, by showing alterations of the transcriptional profiles in various muscle-resident cell types from mdx muscles, in addition to myonuclei and MuSCs (Juban *et al*, 2018; Malecova *et al*, 2018; Tidball *et al*, 2018; Chemello *et al*, 2020; Kim *et al*, 2020).

Pharmacological strategies that target the pathogenic activation of muscle-resident cell types in DMD include the current standard treatment with steroids (Quattrocchi *et al*, 2021), as well as novel

1 Istituto di Ricovero e Cura a Carattere Scientifico (IRCCS), Fondazione Santa Lucia, Rome, Italy
 2 UniCamillus - Saint Camillus International University of Health Sciences, Rome, Italy
 3 Department of Experimental Medicine, University of Rome "La Sapienza", Rome, Italy
 4 Unit of Histology and Medical Embryology, DAHFMO, University of Rome "La Sapienza", Rome, Italy
 5 Department of Drug Chemistry and Technologies, University of Rome "La Sapienza", Rome, Italy
 6 Institute of Nanotechnology (Nanotec), National Research Council (CNR), Rome Unit, Rome, Italy
 7 Development, Aging and Regeneration Program, Sanford Burnham Prebys Medical Discovery Institute, La Jolla, CA, USA
 *Corresponding author. Tel: +39 06 501703266; E-mail: silvia.consalvi@unicamillus.org
 **Corresponding author. Tel: +1 858 6463100; E-mail: lpuri@srbpdiscovery.org
 †These authors contributed equally to this work

interventions with epigenetic drugs, such as histone deacetylase inhibitors (HDACi) (Consalvi et al, 2011). The therapeutic potential of HDACi for DMD has been shown by multiple lines of evidence, including preclinical (Minetti et al, 2006; Consalvi et al, 2013) and early clinical studies (Bettica et al, 2016), and is currently under evaluation in clinical trials with DMD boys (<https://clinicaltrials.gov/ct2/show/NCT03373968>). Studies in mdx mice—the DMD murine model—have shown that the beneficial effects of HDACi are restricted to the early stages of disease progression (Mozzetta et al, 2013; Saccone et al, 2014). This loss of beneficial effects observed in DMD mouse models at late stages of disease suggests that development of a disease-associated resistance might limit the efficacy of HDACi in late-stage DMD patients. Among muscle-resident cells, fibro-adipogenic progenitors (FAPs) have been implicated as central cellular effectors of DMD progression and key targets of the beneficial effects of HDACi in mdx mice (Mozzetta et al, 2013; Saccone et al, 2014). FAPs support muscle-stem cell-mediated repair in acutely injured muscles, but turn into cellular effectors of fibrotic and adipogenic degeneration of muscles exposed to conditions of chronic damage, such as DMD and other neuromuscular disorders (Joe et al, 2010; Uezumi et al, 2010, 2011; Mozzetta et al, 2013; Saccone et al, 2014; Lemos et al, 2015; Kopinke et al, 2017; Madaro et al, 2018; Malecova et al, 2018; Mázala et al, 2020). We have previously shown that in mdx mice at early stages of disease FAPs can promote muscle stem cell (MuSC)-mediated compensatory regeneration and are susceptible to both HDACi-mediated enhancement of their pro-regenerative activity and inhibition of their fibro-adipogenic potential (Mozzetta et al, 2013; Saccone et al, 2014). Moreover, recent studies have revealed that exposure to HDACi promotes the formation and release of pro-regenerative and anti-fibrotic extra-cellular vesicles (EVs) from FAPs of DMD muscles at early stages of disease (Sandona et al, 2020).

The progressive loss of pro-regenerative potential and response to HDACi in FAPs from late-stage mdx mice (Mozzetta et al, 2013) suggests that proportional changes in HDAC activity and related

histone modifications occur in these cells during DMD progression. However, it remains currently unknown whether HDAC activity is altered in FAPs of dystrophic muscles and can generate aberrant profiles of histone acetylation and gene expression; likewise, it is unknown whether these alterations could be effectively restored by HDACi at progressive stages of disease progression and what is their impact on FAP biology.

Results

FAPs of late-stage mdx mice exhibit increased HDAC activity, altered patterns of histone acetylation and partial response to HDACi

We measured class I and class II HDAC activity from lysates of FAPs isolated by FACS (Appendix Fig S1A and B) from hind limb muscles of mdx mice (or control wild-type (wt) mice) at either early (1.5-month-old) or late (12-month-old) stages of disease—hereinafter also referred to as “young mdx FAPs” or “old mdx FAPs”, respectively. Fig 1A illustrates a general and consensual increase in the activity of all HDAC classes—HDAC I, IIa and I/IIb—observed in FAPs isolated from mdx mice, as compared to their wt counterpart. Moreover, while the activity of all classes of HDACs did not change in FAPs isolated from muscles of wt mice at 1.5 or 12 months of age, the enzymatic activity of all HDAC classes was increased about two folds in mdx old FAPs, as compared to mdx young FAPs (Fig 1A). The progressive increase in enzymatic activity observed in in FAPs of mdx, but not wt, mice during aging suggests that deregulation of HDAC activity does not occur as a consequence of chronological aging, but is a disease-associated event. A 15 day treatment with the pan HDACi Trichostatin A (TSA), which we have previously reported to exert histological and functional beneficial effects in young mdx mice (Minetti et al, 2006), could reduce class I HDAC enzymatic activity with a comparable efficacy in mdx FAPs from

Figure 1. Differential patterns of HDAC activity and gene expression in FAPs during DMD progression and treatment with HDACi.

- WY: young wild type; WO: old wild type; YC: young mdx control; YT: young mdx *in vivo* treated with TSA for 15 days; OC: old mdx control; OT: old mdx *in vivo* treated with TSA for 15 days.
- Graphs showing the enzymatic activity of class I (left panel), class IIa (middle panel), and class I/IIb (right panel) HDACs performed in FAPs isolated from WY, WO, YC, YT, OC and OT mice.
 - Cartoon illustrating the experimental strategy. Mdx mice at 1.5 months (young) and 12 months (old) of age were treated with TSA or its vehicle of control for 15 days. At the end of the treatment, FAPs were isolated by FACS from hindlimb muscles to perform H3K9/14ac and H3K27ac ChIP-seq and RNA-seq.
 - Heatmap for H3K9/14ac ChIP-seq signal in the experimental conditions described in B).
 - NGS plot showing H3K9/14ac comparative patterns in the experimental conditions described in B).
 - Heatmap for H3K27ac ChIP-seq signal in the experimental conditions described in B).
 - NGS plot showing H3K27ac comparative patterns in the experimental conditions described in B).
 - Upset graph showing the intersection size (in black) between the differentially acetylated loci for H3K9/14ac (in blue) in the experimental conditions described in B). The top 10 intersections are shown.
 - Upset graph showing the intersection size (in black) between the differentially acetylated loci for H3K27ac (in blue) in the experimental conditions described in B). The top 10 intersections are shown.
 - Heatmap showing 2 clusters of DE genes identified across all the experimental conditions described in B). Gene expression is represented as z-score calculated across the rows.
 - Gene Ontology performed on cluster 1 (left panel) and cluster 2 (right panel) genes.
 - Heatmap showing the differential expression levels by log₂ Fold Change for representative genes of cluster 1 and cluster 2 in the RNA-seq comparisons of YT vs. YC, OC vs. YC and OT vs. OC FAPs.

Data information: In (A) data are presented as average \pm SEM ($n = 4$, biological replicates); (*) indicates statistical analysis by Student's *t*-test in the comparison against WY, $^{***}P \leq 0.0001$, ns = not significant; (*) indicates statistical analysis by Student's *t*-test in the comparison against YC, $^{**}P \leq 0.01$, $^{***}P \leq 0.001$, $^{****}P \leq 0.0001$; (†) indicates statistical analysis by Student's *t*-test in the comparison against OC, $^{\dagger}P \leq 0.05$, $^{****}P \leq 0.0001$; (#) indicates statistical analysis by one-way ANOVA, $^{####}P \leq 0.0001$.

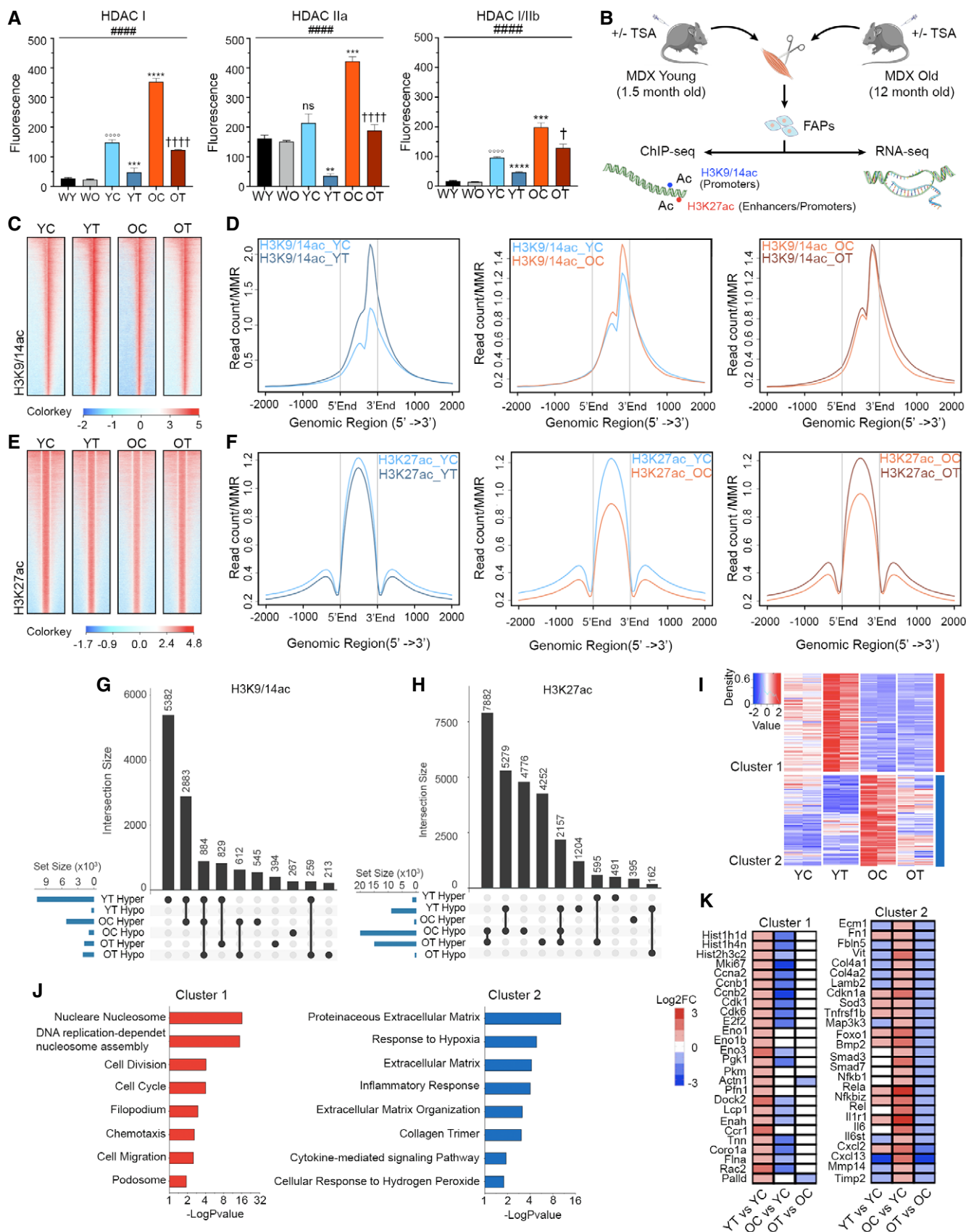


Figure 1.

either stage (Fig 1A, left panel). By contrast, class IIa HDAC activity was drastically inhibited (about 10 fold reduction) by TSA in young mdx FAPs, whereas it was only reduced by half in old mdx mice (Fig 1A, middle panel). Finally, class I/IIb HDAC activity was moderately inhibited by TSA in young mdx FAPs and minimally affected in old mdx FAPs (Fig 1A, right panel). These results show that HDAC activity increases in FAPs of mdx muscles along with disease progression, and that exposure to TSA could reduce the enzymatic activity of class I and II HDAC at both stages, albeit with a progressive reduction in efficacy at late stages that was proportionate to the increased HDAC activity observed in old mdx FAPs.

As HDAC activity controls histone acetylation, we next sought to determine whether the different levels of HDAC activity detected in FAPs from muscles of mdx mice at the two stages of disease (namely, 1.5- or 12-month-old mdx mice) could generate different profiles of genome-wide distribution of histone 3 (H3) acetylation at lysines 9/14 (H3K9/14ac) and lysine 27 (H3K27ac)—two major histone modifications associated with a chromatin conformation permissive for gene expression (Zentner & Henikoff, 2013; Tessarz & Kouzarides, 2014). We also investigated the effect of HDACi on these histone acetylation patterns, by exposing mdx mice to TSA, as described above. In parallel, we performed RNAseq analysis, in order to monitor the transcriptional output of FAPs in the same experimental conditions. Figure 1B illustrates the experimental strategy. ChIP-seq experiments with anti-H3K9/14ac and H3K27ac antibodies revealed distinct profiles of histone acetylation in FAPs isolated from hind limb muscles of young (1.5 month) or old (12 month) mdx mice, either untreated or treated with TSA for 15 days (Fig 1C–F). Global analysis of the cumulative genomic distribution of ChIP-seq peak signals for these histone modifications showed that H3K9/14ac was largely biased toward gene promoters, while H3K27ac signal was distributed between gene promoters (one half) and intronic or distal intergenic elements that typically harbor enhancers (Appendix Fig S1C). This signal is consistent with the enrichment of H3K27ac typically observed at active enhancers and promoters (Hnisz *et al*, 2013; Zentner & Henikoff, 2013; Tessarz & Kouzarides, 2014). Slightly increased genome-wide levels of H3K9/14ac were observed at gene promoters of old mdx FAPs, as compared to young mdx FAPs (Fig 1C and D, middle panel). Interestingly, TSA treatment increased H3K9/14ac signal at gene promoters in young mdx FAPs (Fig 1C and D, left panel), while did not significantly alter the global H3K9/14ac levels at gene promoters in old mdx FAPs (Fig 1C and D, right panel). Conversely, a dramatic loss of H3K27ac acetylation at both gene promoters and outside was observed in old mdx FAPs, as compared to their younger counterpart (Fig 1E and F, middle panel). TSA treatment could recover global H3K27ac acetylation in old mdx FAPs (Fig 1E and F, right panel) to levels comparable to those of young mdx FAPs (Fig 1F, compare middle and right panels). By contrast, TSA decreased H3K27ac signal in young mdx FAPs inside and outside gene promoters (Fig 1E and F, left panel).

Combinatorial intersection of differentially acetylated loci in FAPs across all experimental conditions for both histone modifications shows that the large majority of the H3K9/14ac peaks detected was induced by TSA in young mdx mice, with more than half of them specific for this condition (Fig 1G). Most of the remainder H3K9/14ac peaks induced by TSA in young mdx FAPs coincided with H3K9/14 hyperacetylated loci in old mdx FAPs, with a subset

of them also coinciding with H3K9/14 hypoacetylated loci induced by TSA in old mdx FAPs (Fig 1G). This pattern of combinatorial intersections identifies a putative common subset of gene promoters regulated by H3K9/14 acetylation in both young and old mdx FAPs, whereby common hyperacetylated loci detected in TSA-treated young mdx FAPs and untreated old mdx FAPs coincided with loci hypoacetylated in response to TSA treatment in old mdx FAPs. This specific combination suggests that TSA might differentially affect the H3K9/14ac status of a common subset of gene promoters in FAPs throughout DMD progression. Interestingly, another subset of H3K9/14 hyperacetylated loci uniquely detected in old mdx FAPs coincided with hypoacetylated loci in TSA-treated old mdx FAPs (Fig 1G), further indicating that reversal of H3K9/14 hyperacetylation at gene promoters paradoxically occurs in old mdx FAPs. By contrast, TSA-mediated H3K9/14 hyperacetylation in old mdx FAPs was a rare event and mostly occurred at loci that were also hyperacetylated by TSA in young mdx FAPs (Fig 1G). These data suggest that along with the disease progression in mdx mice, FAPs might develop resistance to HDACi-induced H3K9/14 hyperacetylation, while becoming vulnerable to HDAC-mediated reduction of H3K9/14ac signal at hyperacetylated loci in old mdx FAPs. Conversely, the most dominant combinatorial patterns of H3K27ac included the hypoacetylation at gene loci in old mdx FAPs, with about half of these loci in which H3K27 hyperacetylation was recovered by TSA (Fig 1H). The other half included loci that were also hypoacetylated in young mdx FAPs treated with TSA or loci uniquely detected in old mdx FAPs, in which H3K27ac signal was not recovered by TSA (Fig 1H). This pattern shows that the reduction of H3K27ac in old mdx FAPs can be recovered by TSA at certain loci, but not at others, thereby indicating that old mdx FAPs develop partial resistance to HDACi-mediated H3K27 hyperacetylation. Interestingly, in young mdx FAPs TSA could only reduce H3K27ac, both at unique loci and at loci that were also hypoacetylated in old mdx FAPs (Fig 1H).

HDACi modulate different patterns of gene expression in FAPs of mdx mice at different stages of disease progression

The alterations of the genome-wide histone acetylation profiles detected in FAPs of mdx mice at different stages of disease and in response to TSA predict that consensual alterations in gene expression profiles could also occur in mdx FAPs in the same experimental conditions. We therefore performed RNAseq to analyze the gene expression profile of FAPs isolated from the same experimental conditions described above (illustrated in Fig 1B). Differentially expressed (DE) genes between young and old mdx FAPs were almost equally distributed between up- or downregulated genes (Appendix Fig S2A, middle panel; Appendix Fig S2B). Likewise, TSA induced a similar number of up- and downregulated DE genes in young mdx FAPs (Appendix Fig S2A, left panel; Appendix Fig S2B). In contrast, TSA preferentially downregulated gene expression in old mdx FAPs (Appendix Fig S2A, right panel; Appendix Fig S2B). Combinatorial intersection of DE genes in FAPs across all experimental conditions revealed that the large majority of them was accounted by genes either uniquely up-regulated or downregulated in old mdx FAPs, as compared to their young counterpart; however, while the expression of a proportion of genes upregulated in old mdx FAPs was recovered by TSA-mediated repression, only the expression of very few genes that were downregulated in old

mdx FAPs was recovered by TSA-mediated activation (Appendix Fig S2C). Overall, TSA-modulated genes in young and old FAPs did not show any relevant overlap, suggesting that HDACi modulate different patterns of gene expression in dystrophic FAPs at different stages of disease, as also predicted by their acetylation profiles. Heatmap of top DE genes across all experimental conditions revealed specific patterns of gene expression that could discriminate 2 major clusters of DE genes during FAP transition from an early to a late stage of disease progression in mdx mice, as well as their differential response to TSA (Appendix Fig S3 and Fig 1I). Gene ontology analysis identified specific biological processes for each of these clusters of DE genes. Cluster 1 included a subset of genes whose expression was induced by TSA in young mdx FAPs, but was repressed, and was not recovered by TSA, in old mdx FAPs (Appendix Fig S3 and Fig 1I). Gene ontology assigned these genes to processes related to activation of cell proliferation and migration (Fig 1J). These genes encode cell cycle activators, such as cyclins and cyclin-dependent kinases, histone variants, components of the cytoskeleton as well as activators of glycolysis (Appendix Fig S3 and Fig 1K). Cluster 2 included a subset of genes whose expression increased in old mdx FAPs, as compared to young mdx FAPs; however, TSA treatment could downregulate the expression of these genes to levels comparable to those observed in young mdx FAPs (Appendix Fig S3 and Fig 1I). Gene ontology analysis indicates that this cluster was enriched in genes implicated in regulation of extracellular matrix (ECM), response to hypoxia and inflammation, as well as cytokine-mediated signaling pathways (Fig 1J). Indeed, these genes encode several ligands and receptors for activation of intracellular signaling as well as downstream nuclear transcription factors implicated in ECM remodeling, fibrosis and inflammation (Appendix Fig S3 and Fig 1K).

Altered patterns of H3K9/14ac and H3K27/14ac at promoters of genes implicated in cell cycle arrest and activation of SASP in FAPs of late-stage mdx mice

We next performed an integrated analysis of ChIPseq and RNAseq datasets generated across all experimental conditions to identify

specific patterns of histone acetylation and gene expression that could discriminate young from old mdx FAPs and their different ability to respond to TSA. Specific patterns of histone acetylation were associated to the expression levels of the nearest gene (−1,500/+500 bp distance from the TSS). This analysis revealed two major trends, one consisting of genes that were upregulated in old mdx FAPs and marked by H3K9/14 hyperacetylation at their promoters, another consisting of genes that were downregulated in old mdx FAPs and marked by H3K27 hypoacetylation (Appendix Fig S4A). Gene ontology revealed that upregulated genes marked by H3K9/14 hyperacetylation were enriched in genes belonging to cluster 2 (Appendix Fig S3 and Fig 1I–K) and implicated in ECM remodeling (e.g., TGFbeta signaling) and cytokine-mediated signaling pathways (e.g., TNFalpha or NFkB signaling) (Appendix Fig S4B). Figure 2A illustrates examples of increased H3K9/14ac levels at promoters of representative genes that were upregulated in old mdx FAPs, such as the components of pro-fibrotic TGFbeta signaling, Smad3, Tgfb2 and Tgfb1 (Transforming Growth Factor Beta Induced), (Fig 2A). The upregulation of these representative genes and the increased levels of H3K9/14ac at their promoters in old mdx FAPs, as compared to young mdx FAPs, was validated by independent qPCR (Fig 2B) and ChIP-qPCR (Fig 2C) analyses, respectively. Interestingly, genes upregulated in old mdx FAPs and marked by promoter H3K9/14 hyperacetylation were also enriched in aging process and negative regulation of cell cycle (Appendix Fig S4B). Conversely, genes downregulated in old mdx FAPs and marked by H3K27 hypoacetylation showed enrichment for biological processes related to activation of cell cycle progression, DNA replication and mitosis (Appendix Fig S4C). Figure 2D shows examples of H3K27 hypoacetylation at promoters of representative downregulated genes in old mdx FAPs, such as the cell cycle activators E2F1, Cdk4, and Check2 (Fig 2D). The downregulation of these genes and the decreased levels of H3K27ac at their promoters in old mdx FAPs, as compared to young mdx FAPs, were independently validated by qPCR (Fig 2E) and ChIP-qPCR (Fig 2F) analyses, respectively. These data suggest that FAPs at late stages of DMD progression exhibited some transcriptional features of cellular senescence, such as global activation of secretory pathways and cell cycle arrest. Accordingly,

Figure 2. Integrative analysis of ChIP- and RNA-seq data reveals pathological features reminiscent of cellular senescence in old mdx FAPs.

YC: young mdx control; OC: old mdx control.

- A Acetylation tracks for H3K9/14ac ChIP-seq (on the left) and corresponding FPKM values by RNA-seq (on the right) for representative genes in YC and OC FAPs.
- B Graphs showing RNA levels for the representative genes shown in (A) measured by qPCR.
- C Graphs showing the H3K9/14 acetylation levels for the representative genes shown in (A) measured by ChIP-qPCR.
- D Acetylation tracks for H3K27ac ChIP-seq (on the left) and corresponding FPKM values by RNA-seq (on the right) for representative genes in young and old mdx FAPs.
- E Graphs showing RNA levels for the representative genes shown in (D) measured by qPCR.
- F Graphs showing the H3K27 acetylation levels for the representative genes shown in (D) measured by ChIP-qPCR.
- G Representative images of the EdU staining in freshly isolated YC and OC FAPs following EdU *in vivo* exposure for 3 days (EdU in red/DAPI in blue). Scale bar = 25 μm.
- H Graph showing the percentage of EdU-positive cells for the staining shown in (G).
- I Representative images of the LMNB1 staining in freshly isolated YC and OC FAPs (LMNB1 in green/DAPI in blue). Scale bar = 25 μm.
- J Graph showing the relative quantification of LMNB1 fluorescence intensity normalized for nuclei number, in the staining shown in (I).
- K Graph showing the relative expression of Lmnbl in YC and OC FAPs measured by qPCR.
- L Representative images of the γH2AX and KI-67 staining in freshly isolated YC and OC FAPs (γH2AX in green/KI-67 in red/DAPI in blue). Scale bar = 10 μm. Magnification in the insert (scale bar = 3 μm) shows γH2AX-positive CCF in OC FAPs.
- M Graph showing the percentage of cells positive for γH2AX-positive CCF, for the staining shown in (L).
- N Graph showing the percentage of cells positive for KI-67 for the staining shown in (L).
- O Graph showing the relative expression of Ki67 in YC and OC FAPs measured by qPCR.

Data information: All data are presented as average ± SEM (n = 3, biological replicates); (*) indicates statistical analysis by Student's t-test, *P ≤ 0.05, **P ≤ 0.01, ***P ≤ 0.001, ****P ≤ 0.0001.

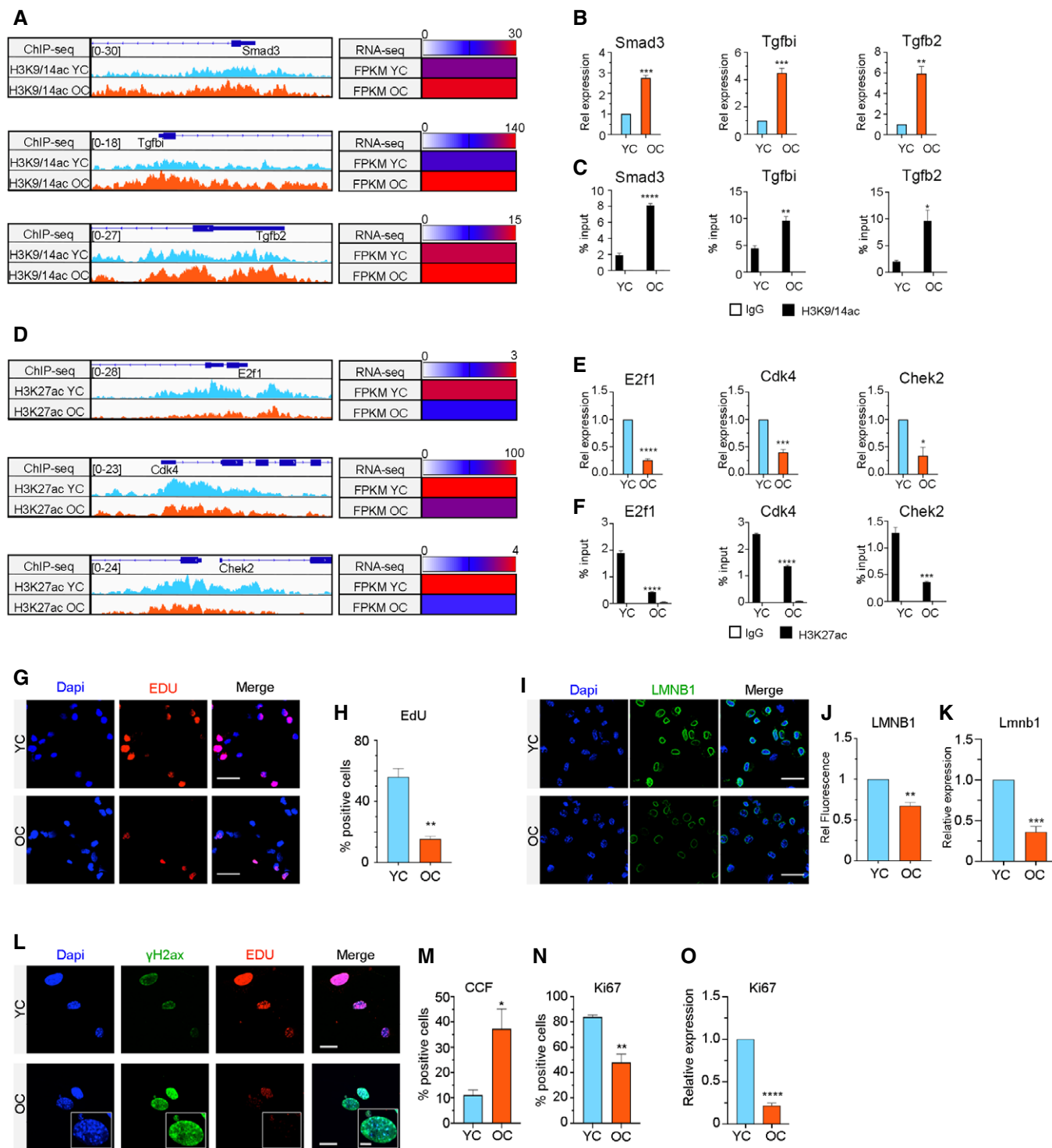


Figure 2.

flow cytometry analysis revealed a drastic decrease of cells progressing through S/G2 phases in old mdx FAPs, as compared to young mdx FAPs. (Appendix Fig S4D and E). Likewise, a drastic decrease of EdU incorporation was observed in old mdx FAPs, as compared to the young counterpart, upon a 3 days *in vivo* exposure to EdU (Fig 2G and H). Furthermore, old mdx FAPs exhibited two

additional features of cellular senescence, such as decreased levels of LaminB1 (LMNB1) (Fig 2I–K) and increased formation of cytoplasmic chromatin fragments (CCF) positive for the DNA damage marker γ H2AX that inversely correlated with the expression of the marker of cell cycle activity Ki67 (Fig 2L–O). Old mdx FAPs also exhibited decreased number of apoptotic cells (Appendix Fig S4F

and G), consistent with the decreased susceptibility to apoptosis of cells upon cell cycle withdrawal.

The transcriptional and biological features reminiscent of cellular senescence observed in FAPs from late-stage mdx mice prompted an interest to determine whether old mdx FAPs indeed undergo cellular senescence. To this end, we initially sought to compare the changes in the transcriptional profile of old mdx FAPs, as compared to old mdx muscle satellite cells (MuSCs), which have been reported to undergo senescence in previous studies (Sacco *et al.*, 2010; Zhang *et al.*, 2016; Latella *et al.*, 2017; Tichy *et al.*, 2017; Chen *et al.*, 2020). We also used macrophages isolated from muscles of mdx mice at the same stages of disease, as a control cell types. We compared RNAseq datasets from these cells and Gene set enrichment analysis (GSEA) revealed that both FAPs and MuSCs (but not macrophages) of late-stage mdx mice exhibited activation of common secretory patterns implicated in Senescence Associated Secretory Phenotype (SASP) and related multiple inflammatory responses (Fig 3A, left panel, and B; Appendix Fig S4H), including the pro-inflammatory cytokine IL-6, which is a typical component of SASP (Appendix Fig S4H and J). Interestingly, these transcriptional features of SASP appeared to be specifically associated to disease progression in mdx mice, rather than being a consequence of chronological aging, as they were not observed in MuSCs and FAPs isolated from age-matched wild-type mice (Fig 3A, right panel). Notably, only MuSCs from late-stage mdx mice expressed specific features of cellular senescence (Fig 3A and C, Appendix Fig S4I), including the upregulation of the conventional senescence marker p16 (Cdkn2a), which was also found upregulated in MuSCs isolated from wild-type geriatric mice, as control (Fig 3D). By contrast, the other senescence-associated cell cycle inhibitor p21 (Cdkn1a) was upregulated in both old mdx FAPs and MuSCs (Fig 3E). Furthermore, old mdx FAPs did not exhibit activation of beta-galactosidase, which was instead induced in old mdx MuSCs, as well as in MuSCs isolated from geriatric mice or human IMR90 fibroblasts induced to undergo replicative senescence, a controls (Fig 3F and G). Finally, a drastic drop in cell number was observed in both old mdx FAPs and MuSCs (Fig 3H; Appendix Fig S4K). Thus, although both MuSCs and FAPs from mdx mice at late stages of disease share common features of senescence, only MuSCs exhibited the conventional markers of cellular senescence, such as upregulation of p16 expression and beta-galactosidase activity.

HDACi downregulate SASP genes by reducing promoter H3K9/14ac in late-stage mdx FAPs

Although cellular senescence is traditionally considered irreversible, once established (Gorgoulis *et al.*, 2019), recent evidence demonstrates that individual biological features of senescence could be reversible (Sinha *et al.*, 2014; Bussian *et al.*, 2018). Thus, we sought to evaluate whether the epigenetic and transcriptional patterns exhibited by old mdx FAPs were reversed, at least partly, by the exposure to the HDACi TSA. In this respect, HDACi have been reported to either promote or counter cellular senescence, depending on the cell type and experimental context (Vizioli *et al.*, 2020). We first evaluated whether TSA could reverse the upregulation of SASP genes in old mdx FAPs. Indeed, the RNAseq expression patterns of cluster 2, which is enriched in SASP genes, shows a consensual downregulation of gene expression levels in FAPs

isolated from old mdx mice treated with TSA (Fig 1I–K; Appendix Fig S3 – right panel). TSA-mediated downregulation of SASP genes invariably coincided with reduction of H3K9/14ac at their promoters, as shown by representative genes implicated in a variety of SASP-related biological processes, including fibrosis (e.g., TGFb-Smad signaling), inflammation (NFkB and p38 signaling) and other components of cytokine- or growth factor-activated pathways, such as IL6, FGF and BMP signaling (Fig 4A; Appendix Fig S5A). The downregulation of these genes and the decreased levels of H3K9/14ac at their promoters in response to TSA were independently validated by qPCR (Fig 4B) and ChIP-qPCR (Fig 4C) analyses, respectively. Consistently, immunofluorescence analysis of muscle sections shows that FAPs (identified as CD90 expressing interstitial cells- Appendix Fig S5B and C) from old mdx mice exhibited the activation of NFkB cascade (as measured by nuclear accumulation of the phosphorylated active form of p65 sub-unit) (Fig 4D and E), p38 pathway (as measured by nuclear accumulation of phosphorylated-p38 alpha kinase) (Fig 4F and G) and TGFb signaling (as measured by nuclear accumulation of phospho-Smad2/3) (Fig 4H and I). Treatment with TSA invariably reduced the activation of all these signaling pathways (Fig 4D–I).

HDACi fail to recover promoter hyperacetylation and expression of cell cycle genes in late-stage mdx FAPs

Conversely, TSA could not resume the expression of genes downregulated in old mdx FAPs and represented in cluster 1, which is enriched in genes implicated in the activation of cell cycle progression (e.g., cyclins, cdks, histones, E2F family members) as well as glycolysis (Fig 1I–K; Appendix Fig S3 – left panel). The common epigenetic features that accompanied the downregulation of these genes during the transition of FAPs from young to old mdx mice was the reduced promoter H3K9/14ac, often in combination with reduced H3K27ac (Fig 5A; Appendix Fig S6A). While TSA could increase H3K9/14 promoter acetylation and expression of cell cycle genes in young mdx FAPs, it failed to recover promoter H3K9/14 hyperacetylation and to resume the expression of these genes in old mdx FAPs (Fig 5A and Appendix Fig S6A and B), as also measured by qPCR and ChIPqPCR analysis at representative genes, such as Hist1h2ae, Cdk1 and CyclinA2 (encoded by Ccna2) (Fig 5B and C). Consistently, the percentage of proliferating cells detected by flow cytometry analysis of Ki-67 expression – a nuclear protein expressed throughout the cell cycle progression, except G0 and early G1 phases – was slightly reduced in old mdx FAPs, as compared to young mdx FAPs (Fig 5D and E – see also Fig 3F; Appendix Fig 4G); however, while TSA could double the percentage of Ki-67-positive FAPs in young mdx mice, old mdx FAPs did not resume the cell cycle in response to TSA treatment (Fig 5D and E). Accordingly, the total number of FAPs was decreased in old mdx mice, as compared to their young counterpart; however, TSA treatment could not increase FAP number at either stage (Fig 5F). The lack of increase in FAP number upon TSA treatment of young mdx mice is apparently in contrast with the increased number of proliferating FAPs detected in TSA-treated young mdx mice. We argue that this discrepancy could be accounted by the increased length of G1-S phase progression observed in TSA-treated young mdx FAPs, due to the activation of a G1/S phase checkpoint by TSA reported by others in several cell types (Gui *et al.*, 2004) and confirmed by our RNAseq

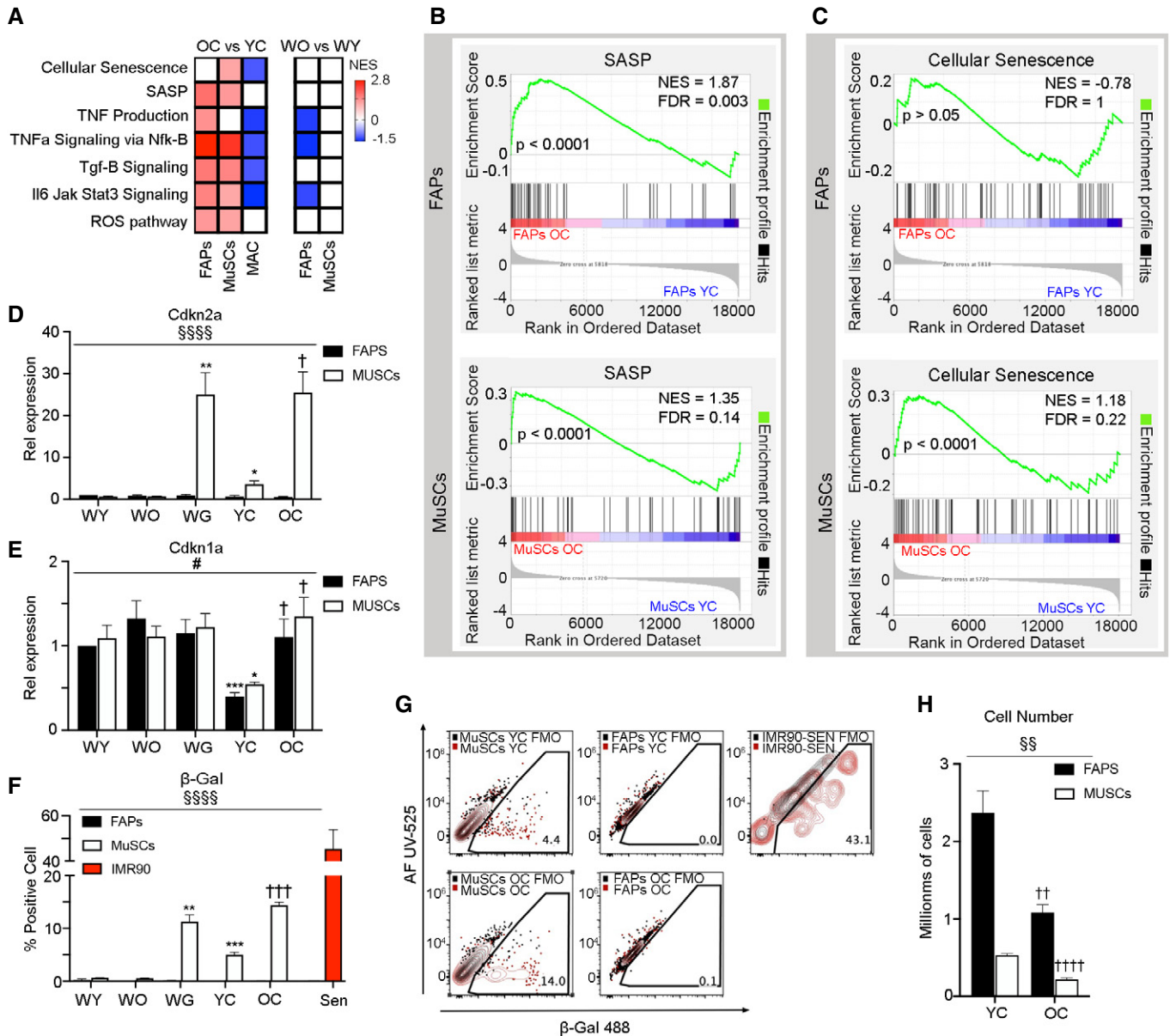


Figure 3. Comparative analysis of FAPs and MuSCs show a different pattern of senescence features.

WY: young wild type; WO: old wild type; WG: geriatric wild type; YC: young mdx control; OC: old mdx control.

A Heatmap showing the normalized enrichment score (NES) measured by GSEA analysis of the listed pathways for FAPs, MuSCs, and Macrophages (MAC) RNAseq in the comparison of OC vs. YC (on the left) and for FAPs and MuSCs in the comparison of WO vs. WY (on the right). GSEA results were filtered for significance by FDR q -value ≤ 0.25 .

B GSEA enrichment plots for gene expression profiles of YC and OC FAPs (on top) and MuSCs (on bottom) against the SASP gene list used in A).

C GSEA enrichment plots for gene expression profiles of YC and OC FAPs (on top) and MuSCs (on bottom) against the Cellular Senescence gene list used in A).

D Graph showing the relative expression of Cdkn1a Cdkn2a in WY, WO, WG, YC, and OC FAPs and MuSCs, measured by qPCR.

E Graph showing the relative expression of Cdkn1a in WY, WO, WG, YC, and OC FAPs and MuSCs, measured by qPCR.

F Graph showing the quantification of β -Gal-positive cells in WY, WO, WG, YC, and OC FAPs and MuSCs compared to late passage IMR90 senescent cells as positive control (SEN) measured by flow cytometry analysis.

G Representative plots of β -Gal 488 fluorescence distribution in YC and OC FAPs and MuSCs and IMR90-SEN cells (in red) compared to their Fluorescence Minus One (FMO) negative control (in black).

H Graph showing the total number of FAPs and MuSCs available in YC and OC single mice.

Data information: All data are presented as average \pm SEM ($n = 3$, biological replicates, in D-G; $n = 4$, biological replicates, in H); (*) indicates statistical analysis by Student's t -test in the comparison against WY, * $P \leq 0.05$, ** $P \leq 0.01$, *** $P \leq 0.001$; (†) indicates statistical analysis by Student's t -test in the comparison against YC, † $P \leq 0.05$, †† $P \leq 0.01$, ††† $P \leq 0.001$, †††† $P \leq 0.0001$; (#) indicates statistical analysis by one-way ANOVA, # $P \leq 0.05$; (§) indicates statistical analysis by two-way ANOVA, §§ $P \leq 0.01$, §§§§ $P \leq 0.0001$.

analysis (see Fig 6B). These data indicate that old mdx FAPs are withdrawn from the cell cycle, a biological feature that is typically associated with an impairment in migratory ability. We therefore analyzed the effect of TSA on FAP migration in young vs. old mdx mice, by a cell migration assay *in vivo*, using FAPs isolated from young or old mdx mice, treated or not with TSA for 15 days. Immediately after isolation, FAPs were labelled with PKH67-488 dye and

transplanted into the proximal part of the gastrocnemius muscle of young mdx mice. 5 days post-injection the number of PKH67-488-positive cells detected in the proximal and distal sections from the injection site were counted by flow cytometry analysis, as readout of their migratory ability. Figure 5 G and H shows that only FAPs isolated from TSA-treated young mdx mice were able to migrate from the proximal injection site to the distal section of

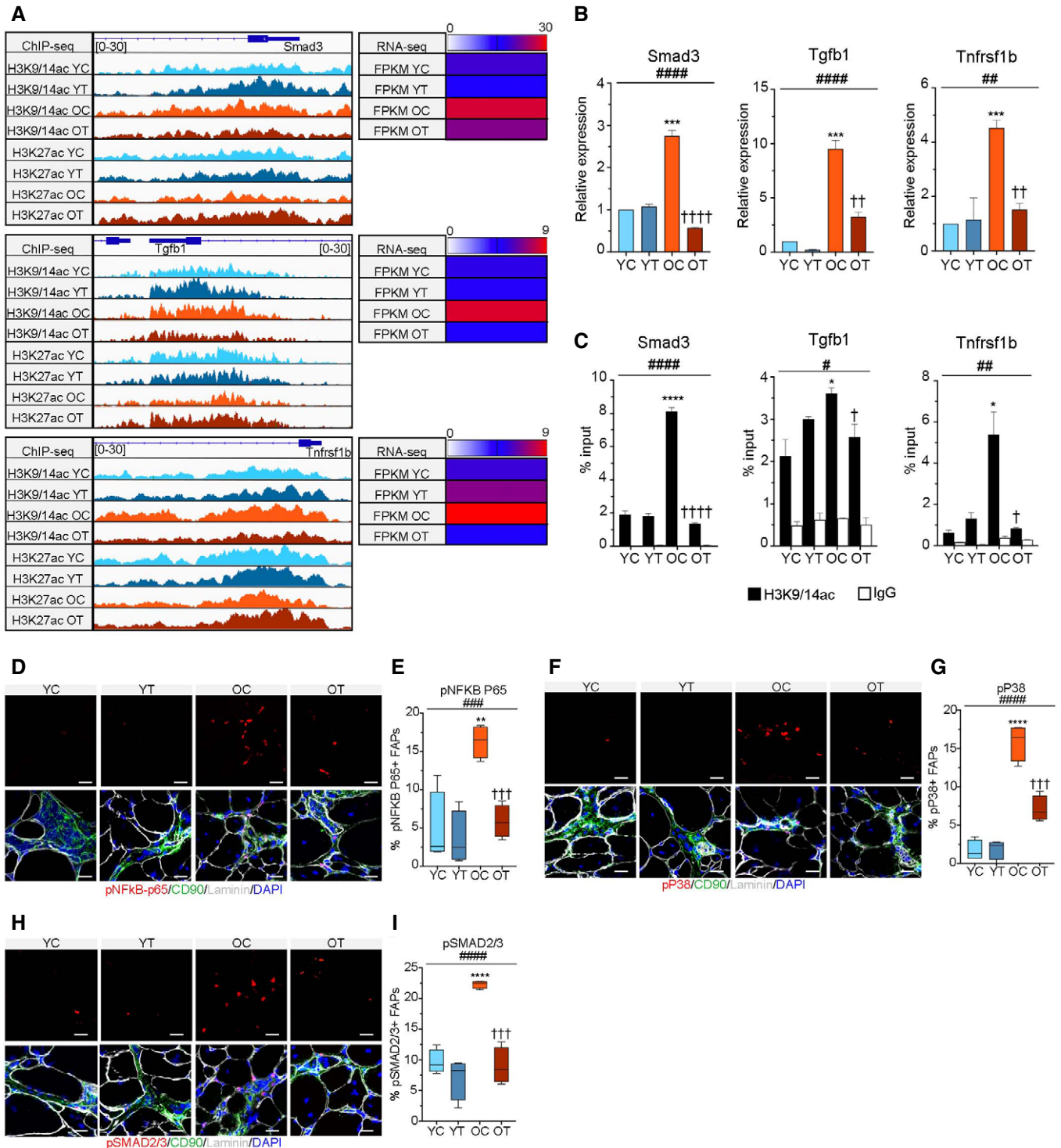


Figure 4.

Figure 4. HDACi reduce the activation of SASP-related signaling pathways in old mdx FAPs.

YC: young mdx control; YT: young mdx *in vivo* treated with TSA for 15 days; OC: old mdx control; OT: old mdx *in vivo* treated with TSA for 15 days.

A Acetylation tracks for H3K9/14ac and H3K27ac ChIP-seq (on the left) and corresponding FPKM values by RNA-seq (on the right) for representative genes in YC, YT, OC, and OT FAPs.

B Graphs showing RNA levels for the representative genes shown in (A) measured by qPCR.

C Graphs showing the H3K9/14 acetylation levels for the representative genes shown in (A) measured by ChIP-qPCR.

D Representative images of the phospho-NFκB staining in FAPs (pNFκB-p65 in red/CD90 in green/Laminin in grey/DAPI in blue) on tibialis anterior muscle transversal section of YC, YT, OC, and OT mice; Scale bar = 25 μm.

E Box plot showing the percentage of pNFκB-p65-positive FAPs in the staining shown in (D).

F Representative images of the phospho-p38 staining in FAPs (pP38 in red/CD90 in green/Laminin in grey/DAPI in blue) on tibialis anterior muscle transversal sections of YC, YT, OC, and OT mice. Scale bar = 25 μm.

G Box plot showing the percentage of pP38-positive FAPs in the staining shown in (F).

H Representative images of the phospho-SMAD2/3 staining in FAPs (pSMAD2/3 in red/CD90 in green/Laminin in grey/DAPI in blue) on tibialis anterior muscle transversal sections of YC, YT, OC and OT mice. Scale bar = 25 μm.

I Box plot showing the percentage of pSMAD2/3-positive FAPs in the staining shown in (H).

Data information: In (B, C) data are presented as average ± SEM, in (E, G, I) the central band of the boxplot shows the median, the box extends from the 25th to 75th percentiles, whiskers are down to the minimum and up to the maximum value ($n = 3$, biological replicates); (*) indicates statistical analysis by Student's *t*-test in the comparison against YC, * $P \leq 0.05$, ** $P \leq 0.01$, *** $P \leq 0.001$, **** $P \leq 0.0001$; (†) indicates statistical analysis by Student's *t*-test in the comparison against OC, † $P \leq 0.05$, †† $P \leq 0.01$, ††† $P \leq 0.001$, †††† $P \leq 0.0001$; (#) indicates statistical analysis by one-way ANOVA, # $P \leq 0.05$, ## $P \leq 0.01$, ### $P \leq 0.001$, #### $P \leq 0.0001$.

gastrocnemius muscles (Fig 5G and H), indicating that old mdx FAPs are refractory to TSA-induced migration. Finally, the observation that the expression of several glycolytic genes, including Eno3 (the muscle-specific isoform of beta-enolase), was repressed in old mdx FAPs and could not be resumed by TSA, which otherwise upregulates these genes in young mdx FAPs (Appendix Fig S3 and S6B), prompted an interest to analyze the ability of FAPs to activate glycolysis in our experimental conditions. Activation of glycolysis could be observed only in FAPs isolated from young mdx mice treated with TSA (Fig 5I). Given the functional interdependence between glycolysis and activation of cell cycle during stem cell activation, and because cell cycle progression and DNA replication favor nuclear reprogramming (Ryall *et al*, 2015), it is likely that the resistance of old mdx to resume expression of cell cycle and glycolytic genes prevents full epigenetic reprogramming by HDACi.

Selective activation of Ox-Phos genes by HDACi via increased promoter H3K27ac in late-stage mdx FAPs

Overall, these data reveal a general trend of loss of response to HDACi-mediated activation of gene expression in old mdx FAPs,

despite these cells retained the ability to downregulate gene expression (e.g., SASP genes) in response to HDACi. This trend is further revealed by a gene ontology analysis of comparative gene expression patterns in FAPs across our experimental conditions, in a graphical representation whereby the size of the bubbles accounts for the number of genes found to be involved in the GO term (Fig 6A). This analysis shows that TSA could both inhibit and promote a variety of cellular processes in young mdx FAPs; however, in old mdx FAPs, TSA activity was only inhibitory toward the biological processes induced in FAPs during DMD progression (Fig 6A). Among them, we noted various processes implicated in fibrosis (e.g., remodeling of extracellular matrix) as well as extracellular exosome formation/secretion. IPA analysis also documented the general trend of inhibition of gene expression by TSA in old mdx mice, with the notable exception of a cluster of TSA-induced genes (cluster 3) implicated in oxidative phosphorylation (Ox-Phos), TCA cycle, electron transport and mitochondrial biogenesis (Fig 6B; Appendix Fig S7A and B). The dominant epigenetic feature of these genes was the H3K27 hypoacetylation at their promoters that accompanied their downregulation in old mdx FAPs, as compared to young mdx FAPs (Fig 6C–E; Appendix Fig S7C). TSA could

Figure 5. FAPs from old mdx mice develop resistance to HDACi-mediated activation of cell cycle.

YC: young mdx control; YT: young mdx *in vivo* treated with TSA for 15 days; OC: old mdx control; OT: old mdx *in vivo* treated with TSA for 15 days.

A Acetylation tracks for H3K9/14ac and H3K27ac ChIP-seq (on the left) and corresponding FPKM values by RNA-seq (on the right) for representative genes in YC, YT, OC, and OT FAPs.

B Graphs showing RNA levels for the representative genes shown in (A) measured by qPCR.

C Graphs showing the H3K9/14 acetylation levels for the representative genes shown in (A) measured by ChIP-qPCR.

D Representative dot-plots of the flow cytometry analysis of KI-67 PE-Cy7 to monitor proliferating YC, YT, OC, and OT FAPs.

E Boxplot showing the percentage of KI-67⁺ FAPs analyzed in (D).

F Boxplot showing the total number of FAPs in the same experimental conditions described in (D).

G Representative dot-plots showing the flow cytometry analysis of FAP migration assay. YC, YT, OC, and OT FAPs were labeled with PKH67-488 and analyzed in the proximal (top panel) and distal (bottom panel) sections from the injection site in YC mice.

H Stacked bar chart showing the relative percentage of PKH67-488⁺ FAPs detected in the proximal (blue) and the distal (red) sections for the same experimental conditions described in (G).

I Histogram showing the level of glycolysis measured by Seahorse as extracellular acidification rate (ECAR) after glucose administration to YC, YT, OC and OT FAPs.

Data information: In (B, C) data are presented as average ± SEM ($n = 3$, biological replicates); in (E, F) the central band of the boxplot shows the median, the box extends from the 25th to 75th percentiles, whiskers are down to the minimum and up to the maximum value ($n = 4$ biological replicates); In (H, I) data are presented as average ± SEM ($n = 4$, biological replicates); (*) indicates statistical analysis by Student's *t*-test in the comparison against YC, * $P \leq 0.05$, ** $P \leq 0.01$, *** $P \leq 0.001$, **** $P \leq 0.0001$, ns = not significant; (#) indicates statistical analysis by one-way ANOVA, # $P \leq 0.01$, ## $P \leq 0.001$, ### $P \leq 0.0001$; (§) indicates statistical analysis by two-way ANOVA, §§§§ $P \leq 0.0001$.

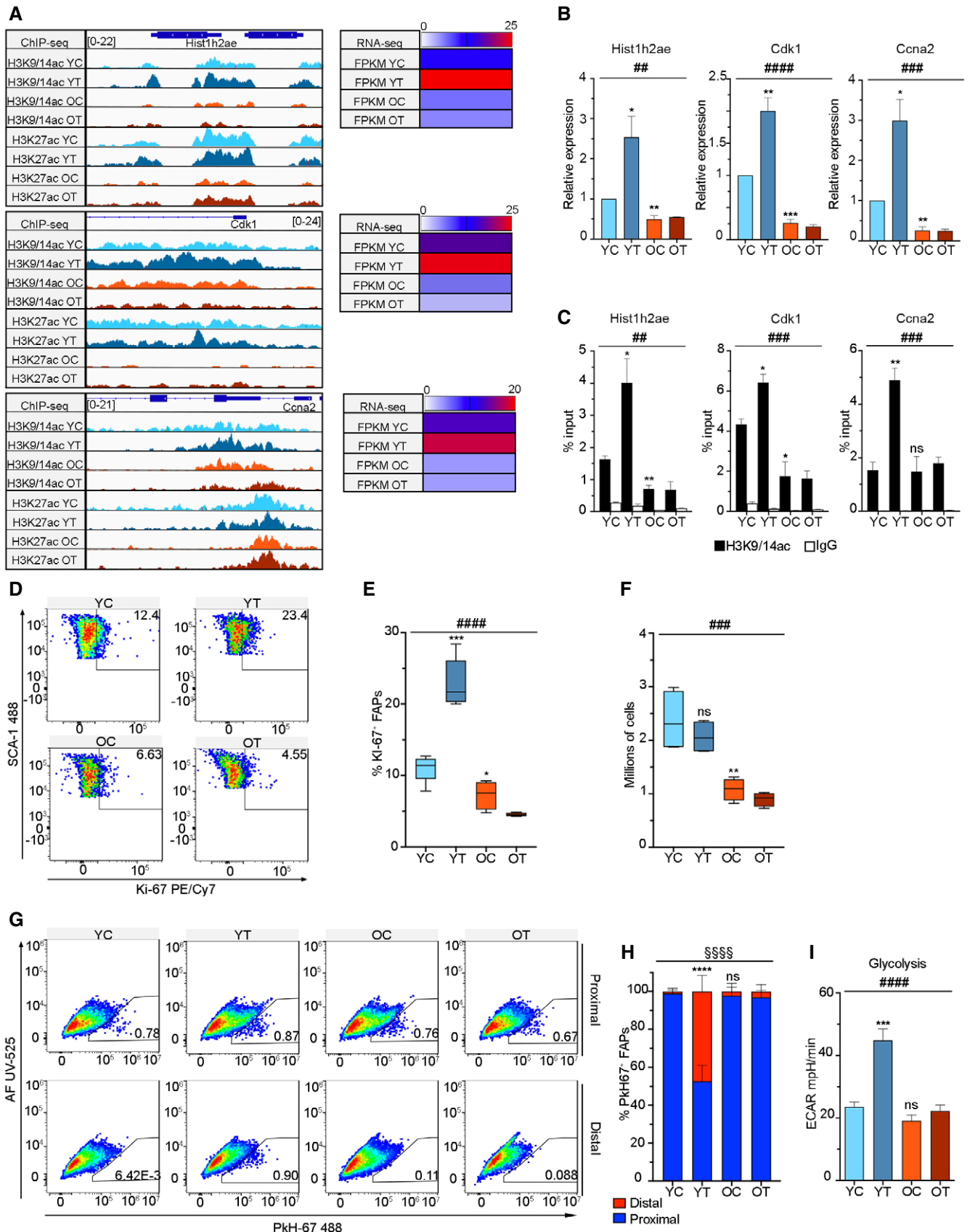


Figure 5.

recover promoter H3K27 hyperacetylation and transcription of these genes in old mdx FAPs (Fig 6C; Appendix Fig S7C). Independent qPCR and ChIPqPCR analysis of representative genes—*Ndufa4*, *Cycs* and *Cox6*—confirmed their downregulation (Fig 6D) and consensual reduction of H3K27ac promoter levels (Fig 6E) in old mdx FAPs and their rescue by TSA treatment (Fig 6D and E). These gene expression patterns were paralleled by coherent changes in mitochondrial activities, with a general trend of reduction of oxygen consumption rate (basal respiration) and ATP production in old mdx FAPs, which was recovered by TSA, albeit not to the levels

observed in TSA-treated young mdx FAPs (Appendix Fig S7D and E). Finally, mitoxox staining detected an increased production of superoxide in old mdx FAPs, as byproduct of dysfunctional mitochondrial oxidative phosphorylation, that was reverted by the exposure to TSA (Appendix Fig S7F and G). Interestingly, the expression of mitochondrial genes was not significantly induced by TSA in young mdx FAPs (Fig 6C–E; Appendix Fig S7C). This suggests that full metabolic reprogramming of young mdx FAPs is induced by TSA by a mechanism distinct from TSA-mediated upregulation of Ox-Phos genes in old mdx FAPs, which results in a slightly increase

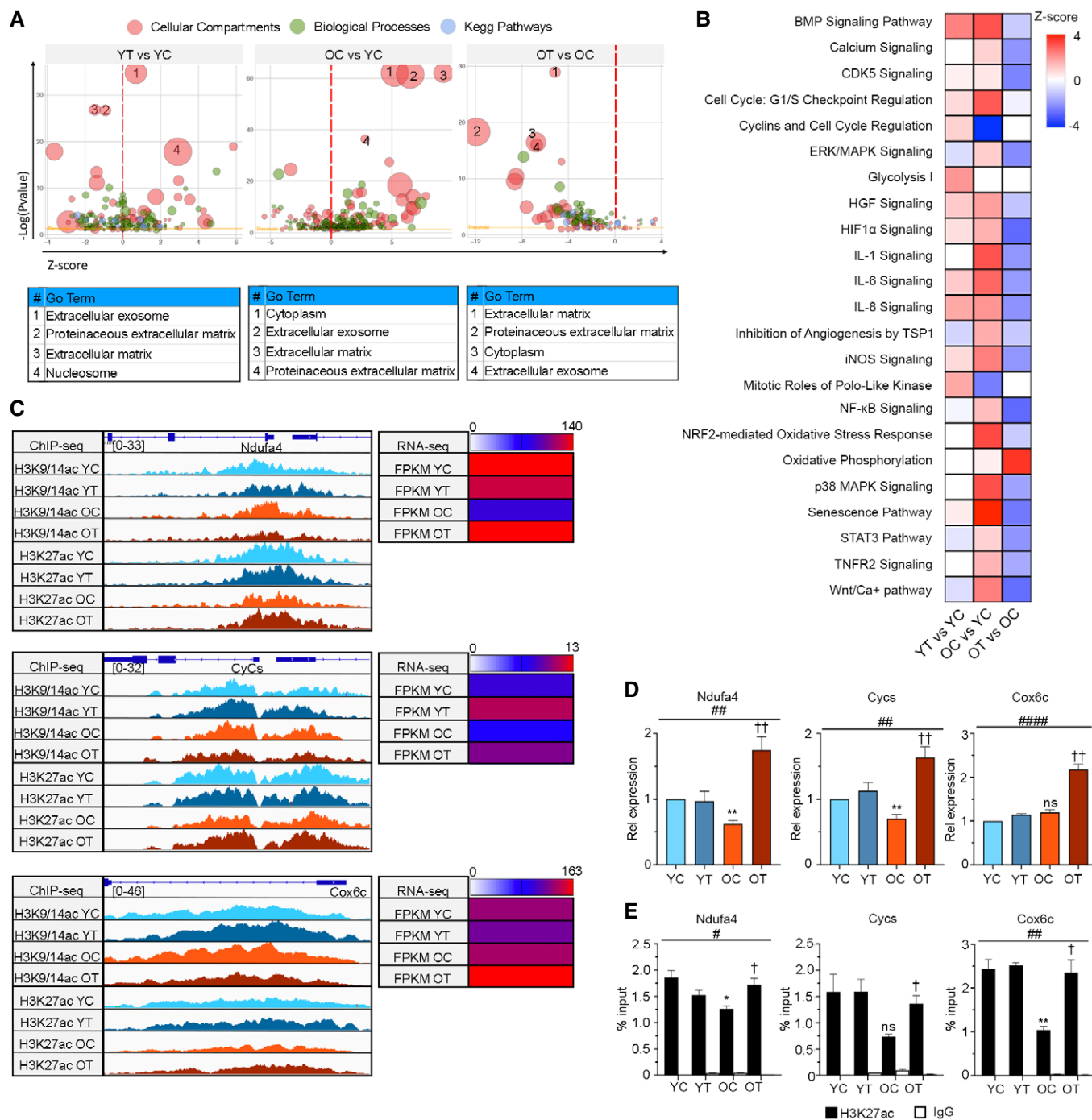


Figure 6.

Figure 6. HDACi recover mitochondrial oxidative phosphorylation in old mdx FAPs.

YC: young mdx control; YT: young mdx *in vivo* treated with TSA for 15 days; OC: old mdx control; OT: old mdx *in vivo* treated with TSA for 15 days.

A Bubble plots showing the Gene Ontology analysis of RNA-seq performed by DAVID in YT versus YC FAPs (left panel), OC versus YC FAPs (middle panel) and OT versus OC FAPs (right panel). The size of the bubbles accounts for the number of genes found to be involved in the GO terms. The top 4 GO terms for each comparison are reported in the table at the bottom.

B Heatmap showing a selection of canonical pathways predicted by IPA in comparative analysis of YT versus YC FAPs, OC versus YC FAPs and OT versus OC FAPs.

C Acetylation tracks for H3K9/14ac and H3K27ac ChIP-seq (on the left) and corresponding FPKM values by RNA-seq (on the right) for representative genes in YC, YT, OC, and OT FAPs.

D Graphs showing RNA levels for the representative genes shown in (C) measured by qPCR.

E Graphs showing the H3K27 acetylation levels for the representative genes shown in (C) measured by ChIP-qPCR.

Data information: In (D, E) data are presented as average \pm SEM ($n = 3$, biological replicates), (*) indicates statistical analysis by Student's *t*-test in the comparison against YC, $^{\dagger}P \leq 0.05$, $^{**}P \leq 0.01$, ns = not significant; (†) indicates statistical analysis by Student's *t*-test in the comparison against OC, $^{\dagger}P \leq 0.05$, $^{**}P \leq 0.01$; (#) indicates statistical analysis by one-way ANOVA, $^{\#}P \leq 0.05$, $^{\#\#}P \leq 0.01$, $^{\#\#\#}P \leq 0.0001$.

of oxidative phosphorylation that might be sufficient to restore mitochondrial dysfunction (Appendix Fig S7D–G).

Discussion

The results shown here revealed that FAPs of mdx mice undergo extensive epigenetic and transcriptional changes during disease progression, leading to two main distinctive biological features—cell cycle arrest and SASP—that discriminate late from early-stage FAPs.

Although cell cycle arrest and SASP are well-known features of cellular senescence (Gorgoulis *et al*, 2019), old mdx FAPs did not exhibit conventional hallmarks of cellular senescence, such as beta galactosidase expression and upregulation of the cyclin-dependent kinase inhibitors 2A (*cdkn2a*) p16. Indeed, the cell cycle arrest observed in old mdx FAPs appears to be caused by a failure to activate the expression of genes implicated in cell cycle progression and DNA synthesis, rather than by the upregulation of p16, as typically observed in cellular senescence. Moreover, SASP activation in old mdx FAPs entails the upregulation of genes encoding for growth factors, cytokines, and other secreted proteins implicated in the regulation of muscle regeneration, inflammation, and ECM remodeling. Some of these genes were already expressed at low levels in young mdx FAPs, and when induced at moderate levels by HDACi some of these genes could promote environmental signals conducive to muscle regeneration—for example, transient inflammation and ECM changes that favor MuSC migration and proliferation. In old mdx FAPs, the simultaneous upregulation and persistent expression of all these genes ultimately leads to fibrosis and inflammation, which negatively impact MuSC-mediated regeneration. Thus, the activation of SASP observed in old mdx FAPs reflects changes in magnitude of transcription of a large collection of genes implicated in regeneration, inflammation, and ECM remodeling.

Previous studies indicated that transient cellular senescence could promote regeneration of skeletal muscle upon acute injury (Chiche *et al*, 2017) or in response to exercise (Saito *et al*, 2020). Conversely, progressive accumulation of senescent cells during chronological aging (Sousa-Victor *et al*, 2014; Chen *et al*, 2020) or upon telomere deficiency (Sacco *et al*, 2010) impairs the regenerative potential of skeletal muscles. We show here that epigenetic and transcriptional features reminiscent of senescence appeared in FAPs from mdx mice as disease progresses. These features were independent on chronological aging and were associated with dysregulated HDAC activity and genome-wide changes of histone acetylation

occurring during disease progression. Treatment with the HDAC inhibitor TSA could inhibit SASP gene activation, by decreasing H3K9/14 acetylation, but did not reverse epigenetic and transcriptional alterations at cell cycle and glycolytic genes. This evidence indicates that during DMD progression FAPs develop resistance to HDACi-induced H3K9/14 hyperacetylation, while remaining vulnerable to HDACi-mediated repression of H3K9/14 acetylation. These data reveal a hitherto unappreciated development of disease-associated features reminiscent of senescence in FAPs of DMD muscles through epigenetically distinct and pharmacologically dissociable events.

Interestingly, cell cycle arrest and activation of SASP in old mdx FAPs were sustained by opposite patterns of histone acetylation. Cell cycle arrest and inhibition of glycolysis were associated with global hypoacetylation at promoters of repressed genes implicated in cell cycle progression, DNA synthesis, and activation of glycolysis. These events are likely accounted by the aberrant activation of HDACs. Indeed, transcriptional repression of these genes was part of a trend of genome-wide H3K27 hypoacetylation in old mdx FAPs that coincided with a general increased HDAC activity and could not be reversed by HDACi. Conversely, activation of SASP genes in old mdx FAPs was sustained by promoter H3K9/14 hyperacetylation and occurred within a trend of H3K9/14 hyperacetylation that was not reversed by HDACi at genome-wide level; however, HDACi could fully repress the activation of SASP genes, by promoting selective H3K9/14 hypoacetylation at their promoters. The genome-wide increase in H3K9/14ac observed in old mdx FAPs is in apparent conflict with the increased HDAC activity. Likewise, the reduction of H3K9/14ac observed at promoters of SASP genes in FAPs of late-stage mdx mice exposed to TSA appears at odd with the expected ability of HDACi to promote hyperacetylation. We argue that these paradoxical effects are likely accounted by the ability of HDACi to target multiple acetylation-dependent and independent events (Wang *et al*, 2009; Greer *et al*, 2015; Sanchez *et al*, 2018; Vaid *et al*, 2020) as well as by the complexity of HDACi activity *in vivo*. Indeed, the final outcome of the systemic exposure of FAPs to HDACi depends on both direct and indirect effects, with the latter likely being generated by signals derived from other muscle-resident cell types that are simultaneously exposed to HDACi. This is particularly relevant for experiments that require long-term exposure to HDACi, as the treatment of mdx mice with TSA. Hence, it is likely that the overall effects of HDACi on genome-wide histone acetylation and transcriptional output in mdx FAPs is determined by modulation of the

heterotypic interactions that FAPs establish with muscle-resident cell types. Conceivably, the senescence-associated features observed in late-stage mdx FAPs might result from functional interactions with other muscle-resident cells implicated in DMD pathogenesis; in turn, FAP-derived SASP can promote the survival or expansion of other cell types that contribute to DMD progression. Therefore, the permanent cell cycle arrest and SASP observed in FAPs at late stages of DMD should be considered as disease-associated features of senescence induced by pathogenic signals released from DMD muscles, rather than conventional features of cell-autonomous activation of cellular senescence. This contention is also supported by the observation that cell cycle arrest and activation of SASP could be already observed in FAPs of mdx mice older than 5 months, but could not be detected in FAPs of aged (older than 2 years) wild-type mice (preprint: Cutler *et al*, 2020).

Overall, the ability of HDACi to promote either moderate and reversible activation of specific SASP genes in young mdx FAPs or global repression of the SASP genes in old mdx FAPs appears a major determinant of the different therapeutical effects of HDACi at early vs. late stages of DMD progression. In particular, the global repression of SASP genes by HDACi in old mdx FAPs might account for the resistance to the pro-regenerative effects of HDACi observed at late stages of disease, but also indicates that HDACi might retain anti-fibrotic and anti-inflammatory effects at late stages of DMD. This therapeutic “trade off” is consistent with a general trend of old mdx FAPs toward a resistance to HDACi-mediated activation of gene expression and release of other secretory signals implicated in muscle regeneration (Fig 6A and B), including release of pro-regenerative EVs (Sandonà *et al*, 2020).

The differential effects of HDACi observed in young vs. old mdx FAPs were associated with their ability to activate cell cycle, glycolysis as well as Ox/Phos metabolism in young, but not old, mdx FAPs. Dysfunctional mitochondrial metabolism has been previously reported in mdx FAPs and correlates with an increased adipogenic potential (Reggio *et al*, 2020). Although HDACi could induce the expression of Ox/Phos genes in old mdx FAPs, this effect was not sufficient to activate basal mitochondrial respiration and ATP production at the extent observed in young mdx FAPs exposed to HDACi (Fig 6 and Appendix Fig S7). Given the intimate link between cell cycle progression, mitochondrial activity, acetyl-coA metabolism and availability of acetyl groups for histone acetylation (Ryall *et al*, 2015; Etchegaray & Mostoslavsky, 2016), it is possible HDACi-mediated activation of cell cycle and mitochondrial activities in young mdx FAPs enable histone hyperacetylation at promoters of genes required for pro-regenerative activities. Conversely, reduced availability of mitochondria-derived acetyl-CoA in old mdx FAPs might limit their ability to respond to HDACi with an increased hyperacetylation at gene promoters. Nonetheless, the HDACi-mediated activation of Ox/Phos genes in old mdx FAPs and repression of SASP genes could be functionally associated, by the suppression of oxidative stress, as recently proposed in models of cellular senescence (Vizioli *et al*, 2020).

Overall, our data provide evidence that cell cycle arrest and SASP are two senescence-associated biological features that limit the response to HDACi in old mdx FAPs. However, their pharmacological dissociation by HDACi (repression of SASP, without reactivation of cell cycle) suggests that HDACi can exert anti-fibrotic and anti-inflammatory effects also at late stages of DMD progression.

Materials and Methods

Animals and *in vivo* treatments

Mice were bred, handled, and maintained according to the standard animal facility procedures and the internal Animal Research Ethical Committee in agreement to the Italian Ministry of Health approved experimental protocols and the ethics committee of the Fondazione Santa Lucia (FSL) approved protocols.

Normal wild-type C57/BL6 and C57Bl6 mdx mice were purchased from Jackson Laboratories. Wild-type C57/BL6 were sacrificed at 1.5, 12 and 30 months of age (respectively defined young, old, and geriatric wt mice). C57Bl6 mdx mice at 1.5 and 12 months of age (respectively defined young and old mdx mice) were treated before the sacrifice for 15 days with daily intra-peritoneal injections of Trichostatin A, TSA (0.6 mg/kg/day; #T8552, Sigma), dissolved in saline solution or in saline alone as vehicle control (CTR).

For Edu assay, 20 µg/kg body weight Edu (#C10351, Invitrogen) was administered by intra-peritoneal injection in young and old mdx mice 3 days before the sacrifice and FAPs isolation.

For the migration assay, FAPs isolated from young or old mdx mice treated or not with TSA were stained with PKH67-488 (#MINI-67, Sigma) immediately after isolation by FACS and injected (20 µl at the concentration of 5000 cells/µl) in the proximal part of the gastrocnemius from the foot-paw of young mdx mice. Mice were sacrificed 5 days postinjection. Gastrocnemius was harvested and cut in half to obtain proximal and distal sections from the injection site. PKH67-488+ FAPs were detected by flow cytometry.

FACS isolation of cells

Muscle-resident cells were isolated from wild-type C57/BL6 and C57Bl6 mdx mice at the end of the treatments immediately after the sacrifice. Hind limb muscles for each mouse were minced and put into a 15 ml tube containing 4 ml of digest solution in HBSS (#24020-091, GIBCO) with 2 mg/ml Collagenase A (#10103586001, Roche), 2.4 U/ml Dispase II (#04942078001, Roche), 10 ng/ml DNase I (#11284932001, Roche) for 90 min at 37°C. Cells were filtered through 100 µm, 70 µm and 40 µm cell strainers (#08-771-19, #08-771-2, #08-771-1, BD Falcon) and resuspended in 0.5 ml of HBSS containing 0.2% w/v BSA and 1% v/v Penicillin–Streptomycin for the staining of cell surface antigens 30 min on ice. The following antibodies were used: CD45-eFluor 450 (1:50, #48-0451-82, eBiosciences), CD31-eFluor 450 (1:50, #48-0311-82, eBioscience), Ter119-eFluor 450 (1:50, #48-5921-82, eBiosciences), Itga7-649 (1:500, #67-0010-01, AbLab), Sca1-FITC (1:50, 5981-82, eBioscience) or Sca1-APC/Fire 750 (1:100, #108145, Biolegend), F480-PE (1:50, #14-4801-81, Thermo Fisher) and CD11b-PECy7 (1:200, #552850, Biosciences).

Cells were finally washed and resuspended in 1 ml of HBSS containing 0.2% w/v BSA and 1% v/v Penicillin–Streptomycin.

Fibro-adipogenic progenitors were purified as Ter119[−]/CD45[−]/CD31[−]/Itga7[−]/Sca1⁺ cells; MuSCs were purified as Ter119[−]/CD45[−]/CD31[−]/Itga7⁺/Sca1[−] cells; Macrophages were purified as Ter119⁺/CD45⁺/CD31⁺/F480⁺/CD11b⁺ cells. Cells were isolated using a Beckman Coulter MoFlo Legacy high-speed cell sorter. Purity check after

cell sorting was performed by flow cytometry (CytoFLEX, Beckman Coulter) and showed purity $\geq 98\%$.

Flow cytometry analysis

Hind limb muscles were digested and the cells were stained with antibodies for cell surface antigens as previously described in the FACS protocol.

For FACS purity check, freshly sorted cells were analyzed by flow cytometry and showed purity $\geq 98\%$. For visualizing cell availability, the same volume (500 μ l) of cells derived from muscle digestion of single young and old mdx mice was acquired for a fixed time window of 180 s by flow cytometry analysis. For CD90 expression analysis, cells from muscle digestion of mdx mice were stained or not (Fluorescence Minus One -FMO) with CD90PE-Cy7 (#140309, Biolegend). For cell cycle analysis, Propidium Iodide (PI) DNA staining was performed (5 μ l of PI and 2.5 μ l of RNase in 500 μ l of PBS, 30 min at 37°C in the dark). For apoptosis analysis, Click-iT. Plus TUNEL Assay (Alexa Fluor™ 594 dye, #C10618, Thermo Fisher) was performed following manufacturer indications. For senescence analysis, Cellular Senescence Detection Kit – SPiDER- β Gal (#SG03-10, Dojindo) was used following manufacturer indications. For cell cycle activation analysis, staining with Ki-67 PE/Cy7 (#652426, Biolegend) was used. For migration assay, total FAPs were detected as Sca1-APC/Fire 750-positive cells (1:100, #108145, Biolegend) and injected FAPs were discriminated as PKH67-488⁺ cells. Cell suspensions were acquired using a CytoFLEX LX flow cytometer (Beckman Coulter) and data were analyzed using FlowJo software (BD Biosciences).

HDAC enzymatic activity assay

Histone deacetylase activity was evaluated by using different fluorogenic substrates specific for class I, class IIa or class I/IIb HDACs (Heltweg *et al*, 2004). The assay was performed as previously described (Lemon *et al*, 2011). Briefly, freshly isolated FAPs were suspended in PBS (pH 7.4) containing 0.5% Triton X-100, 300 mM NaCl and protease/phosphatase inhibitor cocktail (Thermo Fisher Scientific) and sonicated prior to clarification by centrifugation. Protein concentrations were determined using a BCA Protein Assay Kit (Thermo Fisher Scientific). Extracts were diluted into PBS buffer in 100 μ l total volumes in 96-well plate (8 μ g FAPs protein/well). Substrates were added (5 μ l of 1 mM DMSO stock solution), and the plates were returned to the 37°C incubator for 3 h. Then, developer/stop solution was added (50 μ l per well of PBS with 1.5% Triton X-100, 3 μ M TSA, and 0.75 mg/ml trypsin), with additional 20' incubation at 37°C. To detect fluorescent signal Glowmax (Promega) instrument with excitation and emission filters of 360 nm and 460 nm, respectively was used. Background signals from buffer blanks were subtracted.

MitoSOX assay

Freshly isolated FAPs were plated in culture media (BIO-AMF-2, Biological Industries) at high density (3,000 cells, in 96-well dishes). After 24 h FAPs were treated with MitoSOX reagent (Red Mitochondrial Superoxide Indicator, Thermo Fisher, #M36008) and Hoechst 33342 solution (Thermo Fisher, #62249) following the manufacturer

protocols. Images were acquired using Zeiss LSM 800 confocal microscope and quantified using ImageJ software.

Real-time cell metabolic analysis

Mitochondrial function and glycolysis rate were determined using a Seahorse XF96e Analyzer (Seahorse Bioscience – Agilent, Santa Clara CA, USA). FAPs, 10,000 per well, were plated on cell tak (2 μ g per well; Corning) coated Seahorse 96-well utility plate, centrifuged at 1,100 rpm for 10 min at room temperature and held at 37°C in a CO₂-free incubator for 45 min prior to testing.

Mitochondrial function was assessed through a Cell Mito Stress test. Growth medium was replaced with XF test medium (Eagle's modified Dulbecco's medium, 0 mM glucose, pH = 7.4; Agilent Seahorse) supplemented with 1 mM pyruvate, 10 mM glucose and 2 mM L-glutamine. The test was performed by measuring at first the baseline oxygen consumption rate (OCR), followed by sequential OCR measurements after injection of oligomycin (1 μ M), carbonyl cyanide 4- (trifluoromethoxy) phenylhydrazone (1 μ M) and Rotenone (0.5 μ M) + Antimycin A (0.5 μ M) to obtain the key parameters of the mitochondrial function including basal respiration and ATP-linked respiration.

The rate of glycolysis was determined by measuring the rate of extracellular acidification (ECAR). Cells were cultured and pretreated as previously described. The growth medium was replaced with XF test medium (Eagle's modified Dulbecco's medium, 0 mM glucose, pH = 7.4; Agilent Seahorse) supplemented with L-glutamine (1 mM). ECAR was repeatedly evaluated after the injection of glucose (10 mM), oligomycin (1 μ M) and 2D Glucose (50 mM) respectively, in each well.

XF96 data were calculated using the algorithm described and used by the Seahorse software package.

Immunofluorescence

For immunofluorescence on muscle sections, tibialis anterior muscles were snap-frozen in liquid nitrogen-cooled isopentane and then cut transversally with a thickness of 8 μ m. Cryosections were fixed in 4% PFA for 10 min and permeabilized with 0.25% Triton for 15 min at RT. Muscle sections were blocked for 1 h with a solution containing 4% BSA (#A7030, Sigma) in PBS and then incubated with primary antibodies O.N. at 4°C. Antibody binding was revealed using secondary antibodies coupled to Alexa Fluor 488, 594, or 647 (Invitrogen). Sections were incubated 5 min with DAPI in PBS for nuclear staining, washed in PBS, and mounted with glycerol 3:1 in PBS. The primary antibodies used for immunofluorescences were: rabbit anti-Laminin (1:400, #L9393, Sigma), rabbit anti-Phospho-NF κ B p65 (1:1,000, #3033, Cell Signalling), rabbit anti-Phospho-p38 MAPK (1:1,000, #4511, Cell Signalling), rabbit anti-Phospho-Smad2 (Ser465/467)/Smad3 (Ser423/425) (1:1,000, #8828, Cell Signalling) CD90 (1:100, #NB100-65543, Novus Biologicals).

For immunofluorescence on FAPs, freshly isolated cells were seeded by cytospin (1,000 rpm for 5 min at room temperature) on slides and immediately fixed. Immunofluorescence protocol for LMNB1 (1:50, #sc-6216, Santa Cruz) was the same used for muscle sections. For EdU incorporation staining was performed following the manufacturer's instructions (#C10351, Invitrogen). For γ H2AX/KI67 staining, FAPs were seeded in growth media for 24 h in order

to allow cytoplasm flattening and CCF visualization. Immunofluorescence staining was performed as previously by using the primary antibodies: Ser139 H2AX (1:80, Millipore, #05-636) and Ki67 (1:500, #ab15580, Abcam).

Images were acquired using Zeiss LSM 800 confocal microscope and quantified using ImageJ software.

RT-qPCR

Total RNA was extracted from freshly isolated FAPs using TRIzol and 0.5–1 mg were retro-transcribed using the Taqman reverse transcription kit (Applied Biosystems). Real-time quantitative PCR was performed to analyze relative gene expression levels using SYBR Green Master mix (Applied Biosystems) following manufacturer indications. Relative expression values were normalized to the housekeeping gene GAPDH.

Primers sequences are available in Appendix Table S1.

ChIP

C57Bl6 mdx mice (1.5- and 12-month-old) were treated or not with TSA for 15 days and FAPs were freshly isolated by FACS. DNA was double-crosslinked to proteins with 37% formaldehyde (Sigma) at a final concentration of 1%. After incubation for 10 min, glycine was added to give a final concentration of 0.125 M for 5 min. Cells were washed twice with PBS and resuspended in Nuclei Lysis buffer (50 mM Tris-HCl pH 8.1; 10 mM EDTA; 1% SDS and protease inhibitors) for 1 h at +4°C. Chromatin was sonicated to obtain fragments of around 200–300 bp and then diluted 1:10 in IP Dilution buffer (0.01% SDS; 1.1% Triton X-100; 1.2 mM EDTA; 16.7 mM Tris-HCl pH 8.1; 167 mM NaCl). Chromatin extracts were immunoprecipitated overnight on rotating platform at 4°C with anti-H3K27ac (#8173S, Cell Signaling), anti-H3K9/14ac (#C15410005, Diagenode) and normal rabbit IgG (#sc2027, Santa Cruz) as a negative control. For each immunoprecipitation, 10 µl of antibody were used for 100 µg of chromatin. Antibody-bound chromatin was incubated with 50 µl of magnetic beads (G-protein magnetic Beads, Invitrogen) 2 h on rotating platform at 4°C. Chromatin was washed twice with Low Salt buffer (0.1% SDS, 1% Triton, 2 mM EDTA; 20 mM Tris pH 8, 150 mM NaCl), High Salt buffer (0.1% SDS, 1% Triton, 2 mM EDTA; 20 mM Tris pH 8, 500 mM NaCl), Lithium Buffer (0.25 M LiCl; 1% NP40; 1% deoxycholate; 1 mM EDTA; 10 mM Trish pH 8) and TE. Bound DNA fragments were eluted in IP Elution Buffer (1% SDS; 1 mM EDTA; 10 mM Trish pH 8) at 65°C for 15 min and the crosslink was reversed by incubation at 65°C overnight. Proteins were enzymatically digested with proteinase K, 2 h at 37°C, and finally, DNA was extracted with phenol–chloroform. Real-time quantitative PCR was performed using SYBR Green Master mix (Applied Biosystems) following manufacturer indications. Acetylation levels were normalized as percentage of input.

Primers sequences are available in Appendix Table S1.

RNA-seq

RNA was harvested from freshly isolated FAPs, MuSCs, and Macrophages using TRIzol reagent (#T9424, Sigma) and 1 µg (100 ng/µl) was sent to IGA (Istituto di Genomica Applicata, Udine) for RNA

sequencing using Illumina TruSeq Stranded Total RNA kit Ribo-Zero GOLD on Illumina HiSeq2500 platform.

RNA sequencing analysis was performed mapping more than 20 millions of reads for each sample to the Mus Musculus GRCm38.78 genome using TopHat 2.0.9. Read count was performed with HTSeq-0.6.1p1. Mapped reads were analyzed with R-studio (R version 3.5.2) using DESeq2 to obtain differentially expressed (DE) genes with normalized RPKM, p-value, padjusted and log₂fold change values. DE genes were considered differentially expressed for padjusted < 0.1. DE genes were visualized by Heatmaps, MA plots (generated with DESeq2) and Violin plot (generated with Prism 8.0).

DEseq2 differential genes were analyzed for overlap between datasets using the Intervene tool with default parameters. The matrix of overlaps was generated in R 3.5.2 and uploaded in the intervene shiny app (<https://asntech.shinyapps.io/intervene/>) and the Upset graph was generated.

Clusters were manually curated from the total RNA-seq heatmap. For gene ontology DE genes (P -adj < 0.1) were uploaded in <https://david.ncifcrf.gov> and the most relevant GO terms were manually selected. Results were processed in the R package GOplot for the bubble plots. The associated gene expression heatmap was generated by manually selecting the most relevant genes for each biological category from David Gene Ontology. Heatmaps and histograms were generated in GraphPad prism 8.0.

QIAGEN Ingenuity Pathway Analysis (IPA) was performed as comparative analysis of the multiple experimental groups filtering DE genes for P -adj < 0.1. A selection of significant canonical pathways (P < 0.1) was shown as heatmap generated in GraphPad prism 8.0.

Gene set enrichment analysis (GSEA) was performed by weighted enrichment statistic using the following official lists available in the GSEA download section (<http://www.gsea-msigdb.org/gsea/index.jsp>):

Gobp_Cellular_Senescence
Gobp_Tumor_Necrosis_Factor_Superfamily_Cytokine_Production
Hallmark_Tnfa_Signaling_Via_Nfkb
Hallmark_Tgf_Beta_Signaling
Hallmark_Ilg6_Jak_Stat3_Signaling
Hallmark_Reactive_Oxygen_Species_Pathway

GSEA analysis for Senescence Associated Secretory Phenotype was performed using the list of SASP genes (Coppé et al, 2010) filtered for mouse genes.

Gsea results for each comparison were filtered for FDR q -value < 0.25.

ChIP-seq

FAPs were isolated by FACS from 10 C57Bl6J mdx male mice for each experimental condition:

1.5- and 12-month-old mdx mice treated or not with TSA for 15 days. Chromatin Immunoprecipitation was performed on freshly isolated FAPs following the same protocol described in ChIP. About 20 ng of immunoprecipitated DNA was sent to IGA (Istituto di Genomica Applicata, Udine) for ChIP-sequencing on Illumina HiSeq2500 platform.

For ChIP-seq analysis more than 30 millions of reads were aligned to the genome using bowtie-0.12.7 alignment software.

Duplicated reads were removed using samtools1.3. Regions of H3K9/14ac and H3K27ac occupancy were determined using macs2 with a FDR < 0.001 and an ExtSize of 147. Input DNA of each sample was used as the control of the Peak Calling. BlackList regions of the murine genome (ENCFF547MET.bed) were excluded using bedtools software. Significant peaks revealed by macs 2 were further filtered using a threshold of macs_score > 100. Peaks were then processed with Homer to have more than 80 tags. ChIP-seq signal was visualized using NGsplot (heatmaps and average plots) and ChIP-Seeker (genomic distribution).

For differential peak calling, a BedSum file, containing the regions to compare, was generated merging and sorting the two bed files of the samples of interest using bedtools. The same bed files were processed in tagDir using the Homer makeTagDirectory command. Differentially acetylated regions were generated comparing the BedSum file to either tagDir using Homer getDifferentialPeaks command with a fold change > 1.1.

Homer differential peaks were analyzed for overlapping regions using the Intervene tool with default parameters. The matrix of overlaps was uploaded in the intervene shiny app (<https://asntech.shinyapps.io/intervene/>) and the Upset graph was generated.

For integration of differential ChIP-seq peaks with RNAseq, bed files generated by Homer or Intervene were intersected with a bed file containing all the promoter locations of mm10 using BedTools intersect. Peaks on the promoters were filtered in R 3.5.2 with transcripts significantly modulated ($P_{adj} < 0.1$) by RNA-seq.

Bed files of differential ChIP-seq peaks and RNAseq were analyzed for overlapping regions using the Intervene tool with default parameters. The matrix of overlaps was uploaded in the intervene shiny app (<https://asntech.shinyapps.io/intervene/>) and the Upset graph was generated. For the visualization of the genes of interest, ChIP and RNA-seq bam files were uploaded in IGV and the graphic was normalized with the group auto scale option. Coverage signal was used for ChIP-seq and FPKM value was used for RNA-seq.

Statistical analysis

Data are presented as mean \pm SEM. Comparisons between two groups were made using the student's t-test. Comparisons between three or more groups were made using one-way ANOVA when considering only one independent variable. Comparisons between three or more groups were made using two-way ANOVA when considering the effect of two factors on a dependent variable.

Significance is defined as $*P \leq 0.05$, $**P \leq 0.01$, $***P \leq 0.001$, $****P \leq 0.0001$ or analogously for other symbols indicated in the figure legends.

Statistical analysis was performed in PRISM 8.0 (GraphPad Software).

Data availability

The datasets and computer code produced in this study are available in the following databases:

- RNA-Seq data: Gene Expression Omnibus GSE189824 (<https://www.ncbi.nlm.nih.gov/geo/query/acc.cgi?acc=GSE189824>).

- Chip-Seq data: Gene Expression Omnibus GSE189823 (<https://www.ncbi.nlm.nih.gov/geo/query/acc.cgi?acc=GSE189823>).

Expanded View for this article is available online.

Acknowledgments

We thank Giovanna Borsellino and Luca Battistini (Fondazione Santa Lucia, Roma, Italy) for isolation of FAPs by cell sorting and flow cytometry analysis. This work has been supported by the following funding: AFM Telethon #23531 to VM, "Avvio alla ricerca" by Sapienza University of Rome to AR; AFM and DPP_Ita Grants to SC; DPP_Ita PhD fellowship to LT; R01AR076247-01 NIH/NIAMS, MDA 418870 and EPIGEN F7 to PLP

Author contributions

Silvia Consalvi: Conceptualization; Data curation; Formal analysis; Supervision; Project administration. **Luca Tucciarone:** Data curation; Formal analysis; Investigation. **Elisa Macri:** Formal analysis; Investigation. **Marco De Bardi:** Formal analysis. **Mario Picozza:** Formal analysis. **Illari Salvatori:** Formal analysis. **Alessandra Renzini:** Investigation. **Sergio Valente:** Investigation. **Antonello Mai:** Investigation. **Viviana Moresi:** Data curation; Formal analysis; Investigation. **Pier Lorenzo Puri:** Conceptualization; Funding acquisition; Methodology; Writing—original draft; Project administration; Writing—review and editing.

In addition to the CRediT author contributions listed above, the contributions in detail are:

SC and LT performed most of the experimental work. SC performed ChIP-seq and RNA-seq; LT performed bioinformatic analysis; EM contributed to experimental analysis; MDB performed FACS sorting experiments; MP performed flow cytometry analysis; IS performed metabolic assays; VM, AR, SV, and AM performed HDAC activity assay; SC and PLP conceived the project, supervised the study and interpreted the data. PLP wrote the manuscript and all authors discussed the results and commented on the manuscript.

Disclosure and competing interests statement

The authors declare that they have no conflict of interest.

References

- Bettica P, Petrini S, D'Oria V, D'Amico A, Catteruccia M, Pane M, Sivo S, Magri F, Brajkovic S, Messina S *et al* (2016) Histological effects of givinostat in boys with Duchenne muscular dystrophy. *Neuromuscul Disord* 26: 643–649
- Bhat HF, Mir SS, Dar KB, Bhat ZF, Shah RA, Ganai NA (2017) ABC of multifaceted dystrophin glycoprotein complex (DGC). *J Cell Physiol* 233: 5142–5159
- Bussian TJ, Aziz A, Meyer CF, Swenson BL, van Deursen JM, Baker DJ (2018) Clearance of senescent glial cells prevents tau-dependent pathology and cognitive decline. *Nature* 562: 578–582
- Cappellari O, Mantuano P, De Luca A (2020) "The Social Network" and muscular dystrophies: the lesson learnt about the niche environment as a target for therapeutic strategies. *Cells* 9: 1659
- Chamberlain JR, Chamberlain JS (2017) Progress toward gene therapy for duchenne muscular dystrophy. *Mol Ther* 25: 1125–1131
- Chemello F, Wang Z, Li H, McAnally JR, Liu N, Bassel-Duby R, Olson EN (2020) Degenerative and regenerative pathways underlying Duchenne muscular dystrophy revealed by single-nucleus RNA sequencing. *Proc Natl Acad Sci USA* 117: 29691–29701

- Chen W, Datzkiw D, Rudnicki MA (2020) Satellite cells in ageing: use it or lose it. *Open Biol* 10: 200048.
- Chiche A, Le Roux I, von Joest M, Sakai H, Aguin SB, Cazin C, Salam R, Fiette L, Alegria O, Flamant P *et al* (2017) Injury-induced senescence enables *in vivo* reprogramming in skeletal muscle. *Cell Stem Cell* 20: 407–414
- Consalvi S, Mozzetta C, Bettica P, Germani M, Fiorentini F, Del Bene F, Rocchetti M, Leoni F, Monzani V, Mascagni P *et al* (2013) Preclinical studies in the mdx mouse model of duchenne muscular dystrophy with the histone deacetylase inhibitor givinostat. *Mol Med* 19: 79–87
- Consalvi S, Saccone V, Giordani L, Minetti G, Mozzetta C, Puri PL (2011) Histone deacetylase inhibitors in the treatment of muscular dystrophies: epigenetic drugs for genetic diseases. *Mol Med* 17: 457–465
- Constantin B (2014) Dystrophin complex functions as a scaffold for signalling proteins. *Biochim Biophys Acta* 1838: 635–642
- Coppé JP, Desprez PY, Krtolica A, Campisi J (2010) The senescence-associated secretory phenotype: the dark side of tumor suppression. *Annu Rev Pathol* 5: 9–118
- Cutler AA, Pawlikowski B, Wheeler JR, Dalla Betta N, Elston T, O'Rourke R, Jones K, Olwin BB (2020) The regenerating skeletal muscle niche guides muscle stem cell self-renewal. *bioRxiv* <https://doi.org/10.1101/635805> [PREPRINT]
- Ervasti JM (2006) Structure and function of the dystrophin-glycoprotein complex, In *The Molecular Mechanisms of Muscular Dystrophies*. Winder SJ (ed.), pp 1–13., Austin, TX: Landes Bioscience
- Etchegaray JP, Mostoslavsky R (2016) Interplay between metabolism and epigenetics: a nuclear adaptation to environmental changes. *Mol Cell* 62: 695–711
- Garbincius JF, Michele DE (2015) Dystrophin-glycoprotein complex regulates muscle nitric oxide production through mechanoregulation of AMPK signaling. *Proc Natl Acad Sci USA* 112: 13663–13668
- Gorgoulis V, Adams PD, Alimonti A, Bennett DC, Bischof O, Bishop C, Campisi J, Collado M, Evangelou K, Ferbeyre G *et al* (2019) Cellular senescence: defining a path forward. *Cell* 179: 813–827
- Greer CB, Tanaka Y, Kim YJ, Xie P, Zhang MQ, Park IH, Kim TH (2015) Histone deacetylases positively regulate transcription through the elongation machinery. *Cell Rep* 13: 1444–1455
- Gui CY, Ngo L, Xu WS, Richon VM, Marks PA (2004) Histone deacetylase (HDAC) inhibitor activation of p21WAF1 involves changes in promoter-associated proteins, including HDAC1. *Proc Natl Acad Sci USA* 101: 1241–1246
- Hardee JP, Martins KJB, Miotto PM, Ryall JG, Gehrig SM, Reljic B, Naim T, Chung JD, Trieu J, Swiderski K *et al* (2021) Metabolic remodeling of dystrophic skeletal muscle reveals biological roles for dystrophin and utrophin in adaptation and plasticity. *Mol Metab* 45: 101157
- Heltweg B, Dequiedt F, Marshall BL, Brauch C, Yoshida M, Nishino N, Verdine E, Jung M (2004) Subtype selective substrates for histone deacetylases. *J Med Chem* 47: 5235–5243
- Hnisz D, Abraham BJ, Lee TI, Lau A, Saint-André V, Sigova AA, Hoke HA, Young RA (2013) Super-enhancers in the control of cell identity and disease. *Cell* 155: 934–947
- Hoffman EP, Brown RH, Kunkel LM (1987) Dystrophin: the protein product of the Duchenne muscular dystrophy locus. *Cell* 51: 919–928
- Joe AWB, Yi L, Natarajan A, Le Grand F, So L, Wang J, Rudnicki MA, Rossi FMV (2010) Muscle injury activates resident fibro/adipogenic progenitors that facilitate myogenesis. *Nat Cell Biol* 12: 153–163
- Juban G, Saclier M, Yacoub-Youssef H, Kernou A, Arnold L, Boisson C, Ben Larbi S, Magnan M, Cuvellier S, Théret M *et al* (2018) AMPK activation regulates LTBP4-dependent TGF- β 1 secretion by pro-inflammatory macrophages and controls fibrosis in duchenne muscular dystrophy. *Cell Rep* 25: 2163–2176
- Kim M, Franke V, Brandt B, Lowenstein ED, Schöwel V, Spuler S, Akalin A, Birchmeier C (2020) Single-nucleus transcriptomics reveals functional compartmentalization in syncytial skeletal muscle cells. *Nat Comm* 11: 6375
- Kopinke D, Roberson EC, Reiter JF (2017) Ciliary Hedgehog signaling restricts injury-induced adipogenesis. *Cell* 170: 340–351
- Lapidos KA, Kakkar R, McNally EM (2004) The dystrophin glycoprotein complex: signaling strength and integrity for the sarcolemma. *Circ Res* 94: 1023–1031
- Latella L, Dall'Agnese A, Boscolo FS, Nardoni C, Cosentino M, Lahm A, Sacco A, Puri PL (2017) DNA damage signaling mediates the functional antagonism between replicative senescence and terminal muscle differentiation. *Genes Dev* 31: 648–659
- Lemon DD, Horn TR, Cavaasin MA, Jeong MY, Haubold KW, Long CS, Irwin DC, McCune SA, Chung E, Leinwand LA *et al* (2011) Cardiac HDAC6 catalytic activity is induced in response to chronic hypertension. *J Mol Cell Cardiol* 51: 41–50
- Lemos DR, Babaeijandaghi F, Low M, Chang CK, Lee ST, Fiore D, Zhang RH, Natarajan A, Nedospasov SA, Rossi FM (2015) Nilotinib reduces muscle fibrosis in chronic muscle injury by promoting TNF-mediated apoptosis of fibro/adipogenic progenitors. *Nat Med* 21: 786–794
- Madaro L, Passafaro M, Sala D, Etxaniz U, Lugarini F, Proietti D, Alfonsi MV, Nicoletti C, Gatto S, De Bardi M *et al* (2018) Denervation-activated STAT3–IL-6 signalling in fibro-adipogenic progenitors promotes myofibres atrophy and fibrosis. *Nat Cell Biol* 20: 917–927
- Malecova B, Gatto S, Etxaniz U, Passafaro M, Cortez A, Nicoletti C, Giordani L, Torcinaro A, De Bardi M, Bicciato S *et al* (2018) Dynamics of cellular states of fibro-adipogenic progenitors during myogenesis and muscular dystrophy. *Nat Comm* 9: 3670
- Mázala DAG, Novak JS, Hogarth MW, Nearing M, Adusumalli P, Tully CB, Habib NF, Gordish-Dressman H, Chen Y-W, Jaiswal JK *et al* (2020) TGF- β -driven muscle degeneration and failed regeneration underlie disease onset in a DMD mouse model. *JCI Insight* 5: e135703
- Min YL, Bassel-Duby R, Olson EN (2019) CRISPR correction of duchenne muscular dystrophy. *Annu Rev* 70: 239–255
- Minetti GC, Colussi C, Adami R, Serra C, Mozzetta C, Parente V, Fortuni S, Straino S, Sampaolesi M, Di Padova M *et al* (2006) Functional and morphological recovery of dystrophic muscles in mice treated with deacetylase inhibitors. *Nat Med* 12: 1147–1150
- Morikawa Y, Heallen T, Leach J, Xiao Y, Martin JF (2017) Dystrophin-glycoprotein complex sequesters Yap to inhibit cardiomyocyte proliferation. *Nature* 547: 227–231
- Mozzetta C, Consalvi S, Saccone V, Tierney M, Diamantini A, Mitchell KJ, Marazzi G, Borsellino G, Battistini L, Sassoon D *et al* (2013) Fibroadipogenic progenitors mediate the ability of HDAC inhibitors to promote regeneration in dystrophic muscles of young, but not old mdx mice. *EMBO Mol Med* 5: 626–639
- Muntoni F, Torelli S, Ferlini A (2003) Dystrophin and mutations: one gene, several proteins, multiple phenotypes. *Lancet Neurol* 2: 731–740
- Quattrocchi M, Zelikovich AS, Salamone IM, Fischer JA, McNally EM (2021) Mechanisms and clinical applications of glucocorticoid steroids in muscular dystrophy. *J Neuromuscul Dis* 8: 39–52
- Reggio A, Rosina M, Krahmer N, Palma A, Petrilli LL, Maiolatesi G, Massacci G, Salvatori I, Valle C, Testa S *et al* (2020) Metabolic reprogramming of fibro/adipogenic progenitors facilitates muscle regeneration. *Life Sci Alliance* 3: e20200646

- Rugowska A, Starosta A, Konieczny P (2021) Epigenetic modifications in muscle regeneration and progression of Duchenne muscular dystrophy. *Clin Epigenetics* 13: 13
- Ryall JG, Cliff T, Dalton S, Sartorelli V (2015) Metabolic reprogramming of stem cell epigenetics. *Cell Stem Cell* 17: 651–662
- Sacco A, Mourkioti F, Tran R, Choi J, Llewellyn M, Kraft P, Shkreli M, Delp S, Pomerantz JH, Artandi SE et al (2010) Short telomeres and stem cell exhaustion model Duchenne muscular dystrophy in mdx/mTR mice. *Cell* 143: 1059–1071
- Saccone V, Consalvi S, Giordani L, Mozzetta C, Barozzi I, Sandoña M, Ryan T, Rojas-Muñoz A, Madaro L, Fasanaro P et al (2014) HDAC-regulated myomiRs control BAF60 variant exchange and direct the functional phenotype of fibro-adipogenic progenitors in dystrophic muscles. *Genes Dev* 28: 841–857
- Saito Y, Chikenji TS, Matsumura T, Nakano M, Fujimiya M (2020) Exercise enhances skeletal muscle regeneration by promoting senescence in fibro-adipogenic progenitors. *Nat Commun* 11: 889
- Sanchez GJ, Richmond PA, Bunker EN, Karman SS, Azofeifa J, Garnett AT, Xu Q, Wheeler GE, Toomey CM, Zhang Q et al (2018) Genome-wide dose-dependent inhibition of histone deacetylases studies reveal their roles in enhancer remodeling and suppression of oncogenic super-enhancers. *Nucleic Acids Res* 46: 1756–1776
- Sandoña M, Consalvi S, Tucciarone L, De Bardi M, Scimeca M, Angelini DF, Buffa V, D'Amico A, Bertini ES, Cazzaniga S et al (2020) HDAC inhibitors tune miRNAs in extracellular vesicles of dystrophic muscle-resident mesenchymal cells. *EMBO Rep* 21: e50863
- Serrano AL, Muñoz-Cánoves P (2017) Fibrosis development in early-onset muscular dystrophies: Mechanisms and translational implications. *Semin Cell & Dev Biol* 64: 181–190
- Sinha M, Jang YC, Oh J, Khong D, Wu EY, Manohar R, Miller C, Regalado SG, Loffredo FS, Pancoast JR et al (2014) Restoring systemic GDF11 levels reverses age-related dysfunction in mouse skeletal muscle. *Science* 344: 649–652
- Sousa-Victor P, Gutarra S, García-Prat L, Rodríguez-Ubreva J, Ortet L, Ruiz-Bonilla V, Jardí M, Ballestar E, González S, Serrano AL et al (2014) Geriatric muscle stem cells switch reversible quiescence into senescence. *Nature* 506: 316–321
- Tessarz P, Kouzarides T (2014) Histone core modifications regulating nucleosome structure and dynamics. *Nat Rev Mol Cell Biol* 15: 703–708
- Tichy ED, Sidibe DK, Tierney MT, Stec MJ, Sharifi-Sanjani M, Hosalkar H, Mubarak S, Johnson FB, Sacco A, Mourkioti F (2017) Single stem cell imaging and analysis reveals telomere length differences in diseased human and mouse skeletal muscles. *Stem Cell Reports* 9: 1328–1341
- Tidball JG, Welc SS, Wehling-Henricks M (2018) Immunobiology of inherited muscular dystrophies. *Compr Physiol* 8: 1313–1356
- Uezumi A, Fukada S, Yamamoto N, Takeda S, Tsuchida K (2010) Mesenchymal progenitors distinct from satellite cells contribute to ectopic fat cell formation in skeletal muscle. *Nat Cell Biol* 12: 143–152
- Uezumi A, Ito T, Morikawa D, Shimizu N, Yoneda T, Segawa M, Yamaguchi M, Ogawa R, Matev MM, Miyagoe-Suzuki Y et al (2011) Fibrosis and adipogenesis originate from a common mesenchymal progenitor in skeletal muscle. *J Cell Sci* 124: 3654–3664
- Vaid R, Wen J, Mannervik M (2020) Release of promoter-proximal paused Pol II in response to histone deacetylase inhibition. *Nucleic Acids Res* 48: 4877–4890
- Verhaart IEC, Aartsma-Rus A (2019) Therapeutic developments for Duchenne muscular dystrophy. *Nat Rev Neurol* 15: 373–386
- Vizioli MG, Liu T, Miller KN, Robertson NA, Gilroy K, Lagnado AB, Perez-Garcia A, Kiourtis C, Dasgupta N, Lei X et al (2020) Mitochondria-to-nucleus retrograde signaling drives formation of cytoplasmic chromatin and inflammation in senescence. *Genes Dev* 34: 428–445
- Wang Z, Zang C, Cui K, Schones DE, Barski A, Peng W, Zhao K (2009) Genome-wide mapping of HATs and HDACs reveals distinct functions in active and inactive genes. *Cell* 138: 1019–1031
- Zentner GE, Henikoff S (2013) Regulation of nucleosome dynamics by histone modifications. *Nat Struct Mol Biol* 20: 259–266
- Zhang H, Ryu D, Wu Y, Gariani K, Wang X, Luan P, D'Amico D, Ropelle ER, Lutolf MP, Aebersold R et al (2016) NAD⁺ repletion improves mitochondrial and stem cell function and enhances life span in mice. *Science* 352: 1436–1443



License: This is an open access article under the terms of the Creative Commons Attribution-NonCommercial-NoDerivs 4.0 License, which permits use and distribution in any medium, provided the original work is properly cited, the use is non-commercial and no modifications or adaptations are made.